

University of Alberta

**Effects of *In-Situ* Temperature Control on the Nanostructure of
Glancing Angle Deposition Thin Films**

by

Graham Andrew Hunt

A thesis submitted to the Faculty of Graduate Studies and Research
in partial fulfillment of the requirements for the degree of

Master of Science

in

Microsystems and Nanodevices

Department of Electrical and Computer Engineering

©Graham Andrew Hunt

Fall 2013

Edmonton, Alberta

Permission is hereby granted to the University of Alberta Libraries to reproduce single copies of this thesis and to lend or sell such copies for private, scholarly or scientific research purposes only. Where the thesis is converted to, or otherwise made available in digital form, the University of Alberta will advise potential users of the thesis of these terms.

The author reserves all other publication and other rights in association with the copyright in the thesis and, except as herein before provided, neither the thesis nor any substantial portion thereof may be printed or otherwise reproduced in any material form whatsoever without the author's prior written permission.

Abstract

Glancing angle deposition (GLAD) produces sculptured thin films by utilizing substrate motion to control ballistic shadowing, thereby facilitating columnar growth. GLAD relies on control over the statistical distribution of deposited atoms, which changes as a function of temperature. For this reason, it is important that we gain the ability to control substrate temperature and understand its role in film growth. By doing so we may further refine and expand the capabilities of the GLAD technique.

This thesis begins by summarizing my experience designing a GLAD-compatible system for heating and cooling substrates. An automated heating system using (radiative) lamps was implemented and found to be capable of maintaining substrate temperatures as high as 300 °C. Liquid nitrogen was used to cool rotating substrates to temperatures as low as -50 °C, with heat transfer from a copper cooling block to the substrate holder facilitated by Graphalloy[®] bushings and MoS₂ solid lubricant.

Implementation of the heating system allowed the exploration of the effect of elevated substrate temperature on the column inclination angle of various materials. Results vary with material, exposing the complexity of growth mechanisms.

Finally, heated substrates were leveraged to produce *in situ* Sn seed layers to modify the spacing of subsequently deposited GLAD posts. A linear correlation was shown to exist between the separation distances of the Sn seeds and those of GLAD posts deposited on top of the seeds, indicating an inheritance of seed position by the GLAD structures, and demonstrating this method capable of influencing GLAD post nucleation.

Acknowledgments

I'd like to start by thanking my parents for providing for me as their son, shaping me as a person, and supporting me as a student. Without my family—even my sisters—I would not be where I am today.

Thank you to Dr. Jeremy Sit for recognizing the value of my Materials Engineering background and taking me on as a student. Thank you for giving me the freedom to pursue my interests, while guiding me through my times of difficulty. Most of all, thank you for encouraging me to work hard and get the most out of my graduate experience.

I would also like to thank Dr. Michael Taschuk for mentoring me on the many aspects of research. You are truly gifted in your ability to give just enough of a hint to provide direction, while still allowing me to develop my own abilities. Perhaps even more miraculous, you managed to keep me in line and my project on track, and for that I will forever be grateful. I must also give special thanks to Joshua Laforge for general computer wizardry, and your seemingly endless depths of theoretical knowledge.

My graduate experience would not have been as enjoyable without all of the great people in the ENL and GLAD labs. Thank you to Joshua Siewert for guaranteeing that every day in the lab had at least one moment of hilarity. A big thanks to Allan Beaudry for being an all-around 'bro'. Thanks to both Al Lalany and Ryan Tucker for their denim expertise and for allowing me to feel cooler by association. Steven Jim for being an excellent cubicle neighbour, soccer teammate, and general problem solver. Jason Sorge, Jonathan Kwan, and Anthony Oko for providing Oiler related

distractions. Michael Thomas for the hilarious times at Shambhala. And to the rest of the GLAD group for being ever accommodating as I made a general mess of things.

I would also like to specially thank Dr. Brett for assembling such a wonderful group of people.

Contents

| | |
|---|----|
| Chapter 1 | 1 |
| 1.1 - Motivation..... | 1 |
| 1.2 - Outline of Work..... | 2 |
| Chapter 2 | 4 |
| 2.1 - Glancing Angle Deposition | 4 |
| 2.2 - Diffusion | 11 |
| 2.3 - Nucleation..... | 14 |
| 2.4 - Ostwald Ripening | 17 |
| 2.5 - Heat Transfer | 20 |
| Chapter 3 | 24 |
| 3.1 - Introduction..... | 24 |
| 3.2 - Description of Old System..... | 25 |
| 3.3 - New Heating System..... | 28 |
| 3.4 - New Cooling System..... | 29 |
| 3.5 - Temperature Measurement | 38 |
| 3.6 - Characterization and Calibration..... | 40 |
| 3.7 - Chapter Summary | 41 |
| Chapter 4 | 43 |
| 4.1 - GLAD Depositions..... | 43 |
| 4.2 - Wedge chuck | 43 |
| 4.3 - Image Preparation | 45 |
| 4.4 - Image Data Analysis..... | 47 |
| 4.5 - Chapter Summary | 48 |
| Chapter 5 | 50 |
| 5.1 - Introduction..... | 50 |
| 5.2 - Experimental Setup | 51 |
| 5.3 - Experimental Results | 53 |
| 5.4 - Discussion..... | 56 |
| 5.5 - Chapter Summary | 58 |
| Chapter 6 | 60 |
| 6.1 - Introduction..... | 60 |
| 6.2 - Experimental Setup | 61 |

| | |
|--|----|
| 6.3 - Experimental Results | 65 |
| 6.4 - Discussion..... | 74 |
| 6.5 - Chapter Summary | 77 |
| Chapter 7 | 78 |
| 7.1 - Introduction..... | 78 |
| 7.2 - Design..... | 78 |
| 7.3 - Effect of Temperature on β | 80 |
| 7.4 - GLAD Nucleation..... | 81 |
| Bibliography: | 83 |

List of Tables

Table 4.1: Deposition parameters for respective wedge chuck positions. 45

Table 5.1: Relevant properties of various material used for slanted post deposition. 52

List of Figures

| | |
|--|----|
| Figure 2.1: Diagram of glancing angle deposition system | 5 |
| Figure 2.2: Diagram of ballistic growth process | 6 |
| Figure 2.3: Movchan and Demchishin structure zone model..... | 7 |
| Figure 2.4: Examples of typical GLAD structures | 10 |
| Figure 2.5: Adatom lifetime diagram | 12 |
| Figure 2.6: Young's equation diagram..... | 15 |
| Figure 2.7: Gibbs free energy change for nucleation | 17 |
| Figure 2.8: Two particle dissolution diagram | 19 |
| Figure 2.9: LSW size distribution..... | 20 |
| Figure 2.10: Interfacial heat transfer..... | 23 |
| Figure 3.1: Old temperature control system..... | 27 |
| Figure 3.2: New lamp setup | 29 |
| Figure 3.3: Heat input from crucible | 30 |
| Figure 3.4: New headpiece design..... | 33 |
| Figure 3.5: New cooling block schematic | 35 |
| Figure 3.6: New cooling system setup..... | 37 |
| Figure 3.7: Temperature controller schematic | 39 |
| Figure 4.1: Wedge chuck | 44 |
| Figure 4.2: Image segmentation | 46 |
| Figure 4.3: Particle map..... | 48 |
| Figure 5.1: Heated and unheated slanted posts of various materials | 54 |
| Figure 5.2: α vs β of Ti slanted posts..... | 56 |

| | |
|---|----|
| Figure 6.1.: Autocorrelation test..... | 64 |
| Figure 6.2.: Seed layer material selection..... | 66 |
| Figure 6.3: Sn seed layer size distributions | 68 |
| Figure 6.4: Thickness vs. Substrate Temperature vs. Size of Sn seeds..... | 70 |
| Figure 6.5: SiO ₂ vertical posts deposited on Sn seeds..... | 71 |
| Figure 6.6: Autocorrelation of Sn seed layer | 73 |
| Figure 6.7: Average separation distance of SiO ₂ vertical posts and their corresponding Sn seed layers..... | 74 |

Chapter 1

Introduction:

1.1 - Motivation

As engineers, we utilize our knowledge in mathematics, physics, chemistry and biology to develop technology for a variety of applications. The development of technology is an evolutionary process, whereby more advanced technology is used to gain better scientific understanding, which in turn is leveraged to further extend our technological capabilities. Nanotechnology focuses on the development of devices and structures with key feature sizes on the order of 100 nm or less. At these size scales, conventional fabrication technologies have typically followed a top-down methodology, where structures are formed by patterning layer upon layer of materials.

More recently, bottom-up fabrication techniques have been explored as low-cost alternatives for producing more complex structures. One of these fabrication techniques is glancing angle deposition (GLAD). Using substrate motion control, GLAD manipulates the direction and distribution of incident vapour flux to produce a variety of sculpted-film structures through ballistic shadowing. Under conditions of low adatom mobility, growth is limited to the tops of established nuclei, facilitating the growth of columnar structures.

Temperature is a critical GLAD growth parameter, influencing the energetics of adatom condensation, nucleation, and growth. By controlling substrate temperature, we may influence the motion and eventual distribution of atoms in our films. For this purpose, one of the main aims of this thesis research was to develop an effective

system for heating and cooling substrates while retaining the motion control offered by GLAD.

1.2 - Outline of Work

Chapter 2 presents the theory and background for this thesis. It starts with a more in-depth explanation of the thin film growth and GLAD process, beginning with growth mechanisms and then exploring the structures produced by the technique. Some key characterization work is reviewed and is followed by a summary of GLAD film applications.

As temperature is the central component to this thesis, an extended summary of diffusion processes was warranted, given the direct link between substrate temperature and diffusion rates. I segue from diffusion into nucleation, as it is equally pertinent to my study of substrate temperature effects, particularly in Chapter 6. Also covered is Ostwald ripening, the primary mechanism responsible for the growth of nanoclusters. Finally, to properly understand the requirements of an (ultra-)high vacuum-compatible heating and cooling system, I briefly cover the basics of heat transfer. Special emphasis was placed on the limitations of heat transfer in vacuum.

Chapter 3 follows the process of redesigning the heating and cooling system which was used for the studies detailed in Chapters 5 and 6. I highlight some of the shortcomings of the old system, then present the changes made and show how they are improvements. Characterization and testing of the new heating and cooling is done to show its limitations.

1.2 -Outline of Work

Chapter 4 covers the experimental methods involved with GLAD depositions; specifically the differences between GLAD and conventional e-beam evaporation. Methods for preparing and processing scanning electron microscope images for measurements are described in detail. I also briefly explain the algorithms used to extract size and column spacing data from processed SEM images.

In Chapter 5, I investigate the effects of substrate temperature on column inclination angle by growing slanted post films on both heated and unheated substrates. Metals with low melting temperatures as well as TiO_2 lost definitive columnar structure at elevated substrate temperature. While both Ti and Si retained the slanted post structure at elevated substrate temperature, column inclination angle increased in Ti films with substrate temperature, while remaining unchanged for Si films.

In Chapter 6, I develop a quick and inexpensive method for producing Sn nucleation layers with tuneable size and separation, to be used as seeds for GLAD film growth. Both substrate temperature and nominal film thickness were investigated as parameters for Sn seed deposition. I deposited SiO_2 vertical posts at various thicknesses on Sn seed layers with varying distributions of size and average separation distances. I then compared average separation distance between the vertical posts and the underlying Sn seeds to confirm whether or not the posts inherit the position of the seeds.

Chapter 7 highlights key findings in the thesis, while discussing some of the challenges I encountered. I then offer some suggestions for future work.

Chapter 2

Theory and Background:

This chapter provides a comprehensive explanation of the GLAD technique, as well as the physical and chemical concepts that govern the work done in the remainder of this thesis. These concepts focus on thin film growth mechanisms most pertinent to GLAD films, specifically at the nucleation stage, which is central to this thesis. Heat transfer and the influence of vacuum environments on heat transfer are also discussed.

2.1 - Glancing Angle Deposition

Glancing angle deposition is a physical vapour deposition (PVD) technique offering control over the nanostructure of thin films. GLAD differs from conventional planar deposition by tilting substrates to highly oblique angles to the direction of incoming vapour flux α , in combination with substrate rotation about the azimuthal angle, φ [1]. A typical GLAD setup, complete with the respective angles for tilt and rotation, is depicted in Figure 2.1.

2.1 -Glancing Angle Deposition

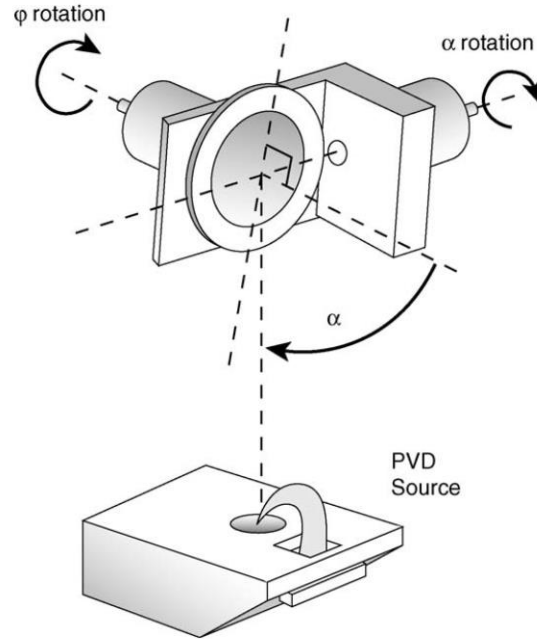


Figure 2.1: Diagram of a conventional glancing angle deposition system. α is the angle formed between the vapour flux and substrate normal that is necessary for shadowing, while φ is the angle of substrate rotation used to control the direction of vapour flux. Reproduced with permission from [2].

Film growth begins with nucleation of small islands of deposited material formed by the agglomeration of atoms in an attempt to minimize free energy in the form of surface bonds [3-5]. By tilting the substrate at highly oblique angles, impinging atoms cannot directly reach areas shadowed by the initial nuclei, thereby limiting further growth to the exposed tops of existing islands [6]. Shadowing therefore results in the growth of columnar structures and highly porous films. This shadowing process is illustrated in Figure 2.2.

2.1 -Glancing Angle Deposition

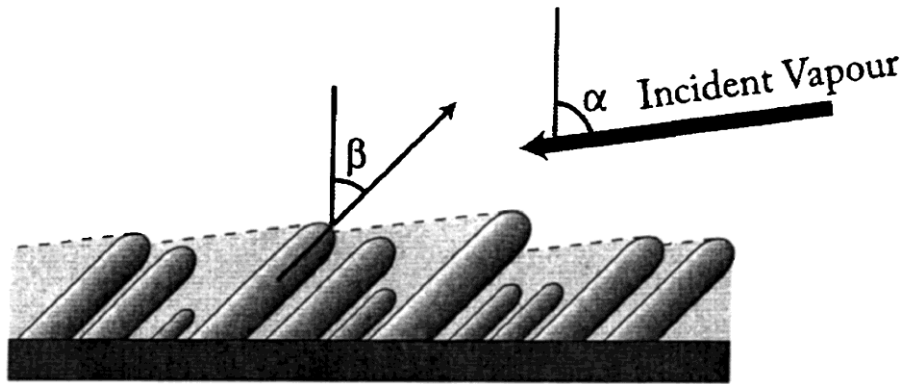


Figure 2.2: Diagram of the ballistic growth process governing the formation of slanted post structures. Vapour flux impinging on the substrate at an angle α is shadowed by already existing structures, which then grow towards the incident vapour at an angle β . Some posts become extinct as they are starved of vapour by faster growing columns. Figure reproduced with permission from [8].

Because this technique is so heavily dependent on the directionality of flux atoms, GLAD is limited to PVD techniques such as evaporation and sputtering [7]. Furthermore, it has been shown that at highly oblique α , even small variations in α can result in very different film growth characteristics, so a more collimated flux is preferred [8]. For this reason, evaporation is the PVD technique of choice for most GLAD applications, rather than sputtering. Sputtering has been enabled through the use of specific techniques such as long-throw sputtering to reduce the flux column spread to a half-width of 8° [9].

PVD thin films have been widely studied to determine suitable growth parameters for use in the microelectronics industry. Generally, suitable films are dense and crystalline with large grains to achieve high electrical conductivities and carrier mobilities [10]. GLAD films instead aim for high porosity and therefore are grown under conditions that are dissimilar to those traditionally used. The structure zone model (SZM) proposed first by Movchan and Demchishin outlines the relation

2.1 -Glancing Angle Deposition

between the ratio of substrate temperature to material melting temperature and the microstructure of the deposited film [11]. Figure 2.3 shows a graphical representation of the structure zone model for evaporated films [12]. It can be seen in Figure 2.3 that, as deposition temperature decreases, so do the film density and crystallinity. More specifically, these lower density films tend to form as columnar structures, suggesting the cause is decreased surface diffusion at low substrate temperatures. After applying the principles of the structure zone model to GLAD films, it is understood that well-defined structures require $T/T_m < 0.3$ [8, 12, 13]. In fact, Sanders proposed a model for evaporation that specifies that nucleate shadowing dominates at $T/T_m < 0.1$ [12].

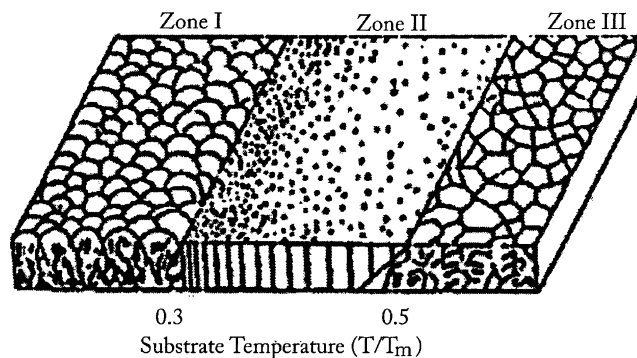


Figure 2.3: Structure zone model for evaporated films, developed by Movchan and Demchishin. Three distinct zones are shown based on the ratio of substrate temperature to deposition material melting temperature (T/T_m): columns separated by voids (Zone I), densely-packed columnar grains (Zone II), and crystalline grains (Zone III). Adapted from [12]

During the columnar growth phase, GLAD films experience a number of phenomena that can have degenerate effects on their structure such as column merging or broadening [1, 14, 15]. Broadening is the tendency for column diameter to increase as the film grows thicker. In past work, this has been attributed to an

2.1 -Glancing Angle Deposition

increase in adatom mobility in response to an increase in temperature during deposition [16]. Because GLAD is typically carried out via evaporation, atoms are transported to the substrate in vapour phase and then condense on the film. The condensation of material imparts latent thermal energy to the substrate and growing film, thereby heating it up and increasing the mobility of adatoms. These adatoms are now able to diffuse distances greater than the diameters of the post and then sorb onto the sides of the columns. As growth continues, this effect is compounded and may result in column merging [8]. Column merging is a phenomenon in GLAD where, during deposition and as columns broaden, some may merge together to form a single column. Column growth can also be competitive, in which certain columns will grow faster and larger than others causing premature termination to many columns. These effects have a tendency to increase column separation, which is often a desirable property of GLAD films [1, 7, 8, 17].

Since the advent of GLAD, a great deal of research has taken place characterizing the growth of GLAD films, including the expansion of the technique to different material groups and a variety of film structures. Structures that are now readily grown include: slanted posts, vertical post, helical posts, screws, zig-zags, square spirals and combinations of the previously mentioned [1, 6]. Slanted posts are grown at high α while maintaining a constant φ . These slanted columns grow towards the incident flux at an angle β from normal to the substrate. This column tilt angle is always less than the angle of incident flux. A simple explanation is that shadowing is only facilitated at impingement angles greater than β , and so growth must occur at smaller angles, otherwise deposition occurs between posts. The relationship between

2.1 -Glancing Angle Deposition

β and α , based on experimental data, was first described by Niewenhuizen and Haanstra in the form of the tangent rule [18, 19]:

$$\tan \alpha = 2 \tan \beta \quad (2.1)$$

The tangent rule, while accurate at lower deposition angles, has been found to become increasingly erroneous at higher α , predicting $\beta = \alpha$ at 90° . For some materials at high deposition angles, β has been empirically determined to most closely follow the relationship described by Tait, *et al.* [20]:

$$\beta = \alpha - \arcsin\left(\frac{1 - \cos \alpha}{2}\right) \quad (2.2)$$

Studies on β have found it to be a function of multiple deposition parameters, including substrate type [21], substrate temperature [22-24], deposition material [22, 25], deposition pressure [22, 26], as well as advanced techniques such as phi-sweep motion control [26], or ion-assisted GLAD [27].

Zig-zag structures are simply slanted posts grown in one direction, then periodically rotated 180° in φ to reverse the direction of the growth front [1].

Screws and helices form as a result of growth at a fixed α , while constantly rotating the substrate about an angle φ . As the substrate is rotated, the growth front follows the incident flux at an angle β and depending on the rate of rotation, forms a helical post. The pitch is the vertical distance between growth fronts along the same plane and is a function of deposition rate and rotation speed. Higher deposition rate and lower rotation speed results in a larger pitch. When the pitch becomes smaller than the post diameter (*i.e.*, at high enough rotation speeds) vertical posts are formed.

2.1 -Glancing Angle Deposition

Square spirals are grown through a modification of the spin-pause technique, where azimuthal rotation is cycled on and off in an attempt to grow slanted posts at a lower β [8]. Unlike the typical spin-pause technique, where rotation is terminated at the same plane each interval, square spirals are formed by rotating the substrate at 90° intervals between long periods of slanted post-like growth. Scanning electron microscope images of each of the films is shown below in Figure 2.4 [1].

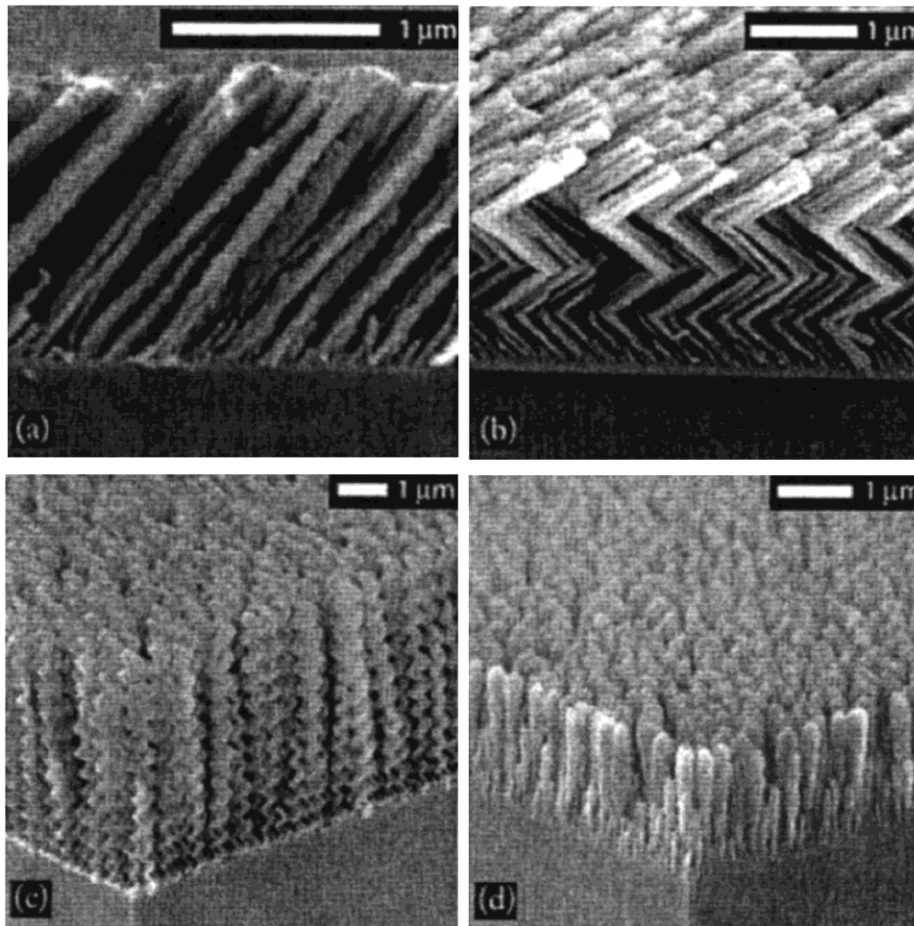


Figure 2.4: Scanning electron microscope images of (a) slanted posts grown at a fixed α without rotation in φ , (b) zig-zag grown by periodically rotating α by 180° without rotation in φ , (c) helices grown at a fixed α with constant rotation in φ , and (d) vertical posts grown in a similar fashion to (c), but with a pitch smaller than the diameter of the post. Reproduced with permission from [8].

2.2 -Diffusion

GLAD films have been used for a variety of applications, specifically for their unique nanostructure. Widely studied is their use for optical devices such as filters and polarizers [28-32]. Another application that has been proposed is the use of GLAD films as high density magnetic storage devices due to the columnar film's natural anisotropy [7, 33-35]. GLAD films have been seen as suitable for these applications due to their intrinsic structural isolation, requiring no patterning or etching for magnetic isolation. One property inherent to GLAD films is their high porosity and therefore high surface area. This makes them ideal sensors for analytes such as $H_2O_{(g)}$. For this reason researchers have come up with GLAD-based humidity sensors. For optical-based GLAD humidity sensors, as water accumulates on the surface of GLAD films, the additional layer of water contributes to a shift in the optical index of refraction. Capacitive humidity sensors detect a change in electrical capacitance as water molecules adsorb on the surface of the GLAD films [37-40]. Another more recent application of GLAD films is for thin layer chromatography (TLC) plates. GLAD TLC plates make use of post anisotropy as well as the high porosity of films to manipulate the mobility of different species and separate analytes, based on their differential affinities to the stationary and mobile phases [41-42]. The improved selectivity of GLAD based TLC plates over conventional TLC makes for a promising area of research. GLAD films have also found a home in photovoltaics, where they have been shown to improve efficiency by structuring electrodes; improving exciton recombination rates or optical absorption [43-47].

2.2 - Diffusion

Thin film growth begins with vapour-phase atoms impinging on a substrate surface, with physical and chemical phenomena governing whether they physisorb onto the

surface, re-evaporate back into vapour phase, or chemisorb at the surface and become part of the thin film structure.

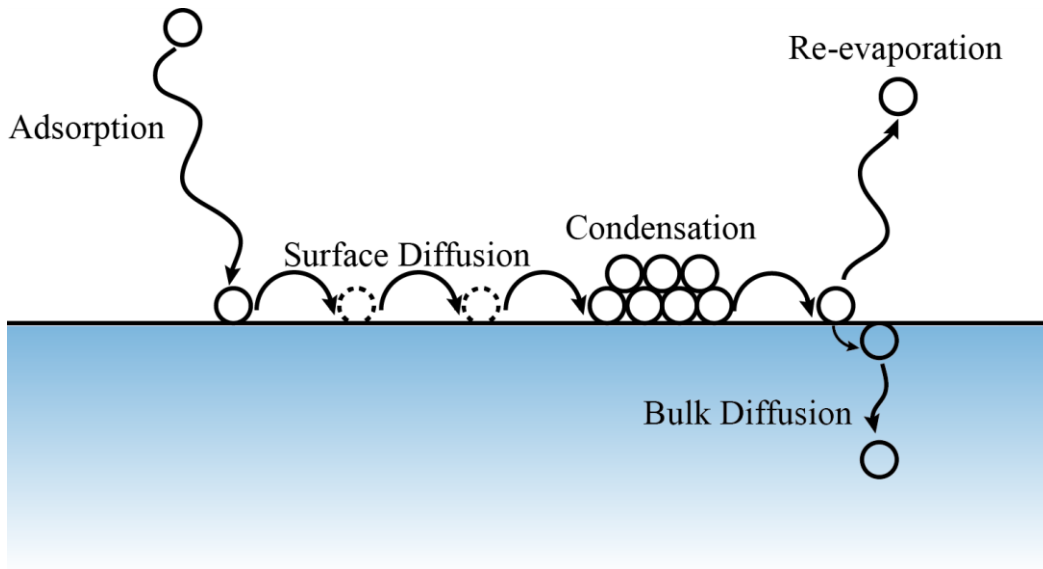


Figure 2.5: Depiction of the possible processes involved during an adatom's lifetime [48].

Figure 2.5 depicts the various states an atom may occupy in close proximity with a substrate surface. When occupying either a physisorbed or chemisorbed state, an atom is able to lower its energy by E_p or E_c respectively. In order for a physisorbed atom to become chemisorbed it must overcome an activation energy barrier, E_a [48-50]. Once a vapour-phase atom is physisorbed, it becomes an adatom. Adatoms are highly energetic atoms that periodically hop between low energy surface sites, losing energy with each jump until they either lower their energy to a point where the atom may chemisorb with the surface, diffuse into the bulk structure, or desorb completely. This random hopping is governed by the energy of the adatom as well as surface conditions such as temperature and the nearest neighbour bonding energy

[51]. Collecting these parameters into a single entity, the one dimensional diffusivity of a species is approximated by [52, 53]:

$$D = D_o \exp\left(\frac{-E_a}{kT}\right), \quad (2.3)$$

where D_o is the temperature-independent diffusivity of the atomic species, E_a is the activation energy for diffusion determined by nearest neighbour bond energy, k is Boltzmann's constant, and T is temperature. This Arrhenius-like expression demonstrates an exponential relationship between adatom mobility and temperature, where higher temperature results in greater mobility. Another conclusion that can be drawn is the material dependency of activation energy. Because activation energy depends on the nearest-neighbour bond strength, which in turn is closely related to the melting temperature T_m , it can be inferred that lower melting temperature materials with lower bond strength will demonstrate a greater propensity to diffuse [15, 52, 53, 54].

While adatom energy and surface conditions are strong indicators of how far an adatom can diffuse, growth kinetics may instead be the limiting factor. An adatom remains on a surface for an amount of time τ_s , determined by [56]:

$$\tau_s = \frac{1}{\omega} \exp\left(\frac{E_s}{kT}\right), \quad (2.4)$$

where ω is the lattice vibration frequency, E_s is the activation energy for surface diffusion, and k and T are as previously defined in Equation 2.3. This average residence time, however, does not take into account the chance that an adatom may be buried by subsequent deposition. For this case, it is assumed that on average, the

2.3 -Nucleation

distance an adatom may diffuse is a function of the ratio of time a monolayer of new material takes to be deposited to the time an adatom may remain mobile on the surface; written as

$$\Lambda = \frac{1}{2} a_h \sqrt{\frac{\tau_m}{\tau_s}}, \quad (2.5)$$

where Λ is the average diffusion distance of an adatom before becoming buried, a_h is the average diffusion distance an adatom may travel unabated, while τ_s and τ_m are the mean diffusion time and mean monolayer formation time respectively [56]. Monolayer formation time decreases linearly with deposition rate and $\Lambda \sim \tau_m^{1/2}$, meaning that the average adatom diffusion distance also scales with $\tau_m^{1/2}$. We see that, as temperature increases, so too does the average diffusion distance, as τ_s decreases with increasing temperature. It also becomes apparent that increasing the deposition rate, and subsequently decreasing monolayer formation time, has the opposite effect on Λ [56].

While bulk diffusion shares with surface diffusion the Arrhenius-like relationship between diffusivity and temperature, bulk diffusion is governed by a volumetric reduction in free energy in an attempt to achieve the lowest energy configuration of atoms within a structure [52].

2.3 - Nucleation

As impinging vapour-phase atoms continue to physisorb onto the substrate surface, they populate the surface with adatoms until supersaturation is reached [48, 55, 57]. This supersaturation of the adatom phase leads to an increased probability of two or more adatoms coming together to form small clusters and lower their energy

2.3 -Nucleation

configuration through a reduction in open bonds. These clusters either dissolve back into the saturated adatom phase or continue to grow until nuclei of stable size are formed, as determined by the relative energies between the vapour phase, condensed phase, and substrate surface [58]. Vapour-phase atoms have more open bonds and are therefore more energetic than atoms in a liquid phase, while atoms at the surface of a condensed droplet are more energetic than those in the bulk of the substrate for the same reason. This difference in bonding energy is represented as interfacial or surface energy. Therefore, the formation of a condensed droplet on the substrate surface creates two new interfaces: the liquid-vapour interface with energy γ_{lv} , and the solid-liquid interface with energy γ_{sl} . These two interfaces combined with the already present solid-vapour interface of energy, γ_{sv} , to form the relationship known as Young's equation, shown in Figure 2.6 below, where θ is the contact angle between liquid-vapour and solid-liquid interfaces [55, 59].

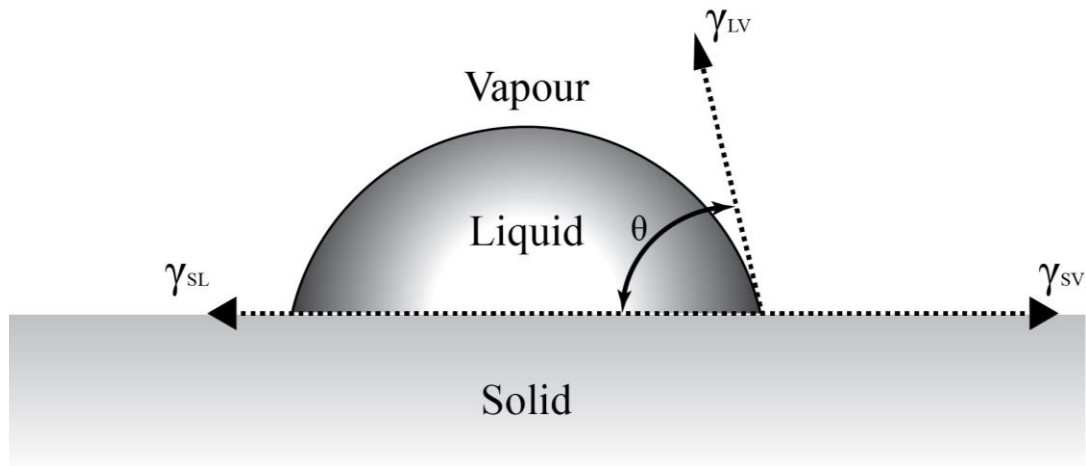


Figure 2.6: Diagram of a liquid droplet in contact with a solid surface. γ_{sv} , γ_{sl} , and γ_{lv} are the energies of the solid-vapour, solid-liquid, and liquid-vapour interfaces, respectively. θ is the contact angle formed by the liquid droplet and can be calculated through application of Young's equation.

2.3 -Nucleation

Another change in energy during condensation of the vapour phase is a reduction of volumetric Gibbs free energy due to the bonding established in the droplet, represented as [49, 60]:

$$\Delta G_v = \frac{k_B T}{\Omega} \ln \left(\frac{P_v}{P_s} \right). \quad (2.6)$$

Here, Ω is the atomic volume of the established nucleus, P_v is the pressure of the supersaturated vapour, and P_s is the pressure above the solid. From Equation 2.6, we can see that supersaturation is required for a negative ΔG_v and therefore a driving force for nucleation, while at the same time, an increasing T will linearly increase that driving force.

The total Gibbs free energy change brought about by condensation of a vapour phase is therefore the sum of the reduction in volumetric free energy and the creation of interfacial energy. A net reduction in free energy is required for the established nuclei to remain stable, and so the condensed droplet assumes a spherical shape to minimize the surface area to volume ratio, as demonstrated in Figure 2.6. Including the terms for spherical geometries yields the total free energy change for a condensed nucleus given by Equation 2.7 below, where ΔG , ΔG_v , and Υ_{sv} are the total free energy change, the volumetric free energy change, and the solid-vapour interfacial energy, respectively [48, 49, 55, 60, 61].

$$\Delta G = \frac{4}{3} \pi r^3 \Delta G_v + 4 \pi r^2 \Upsilon_{sv} \quad (2.7)$$

2.4 -Ostwald Ripening

The total Gibbs free energy for the formation of a nucleus of increasing radius is shown in Figure 2.7, along with plots for the volumetric and interfacial contributions alone.

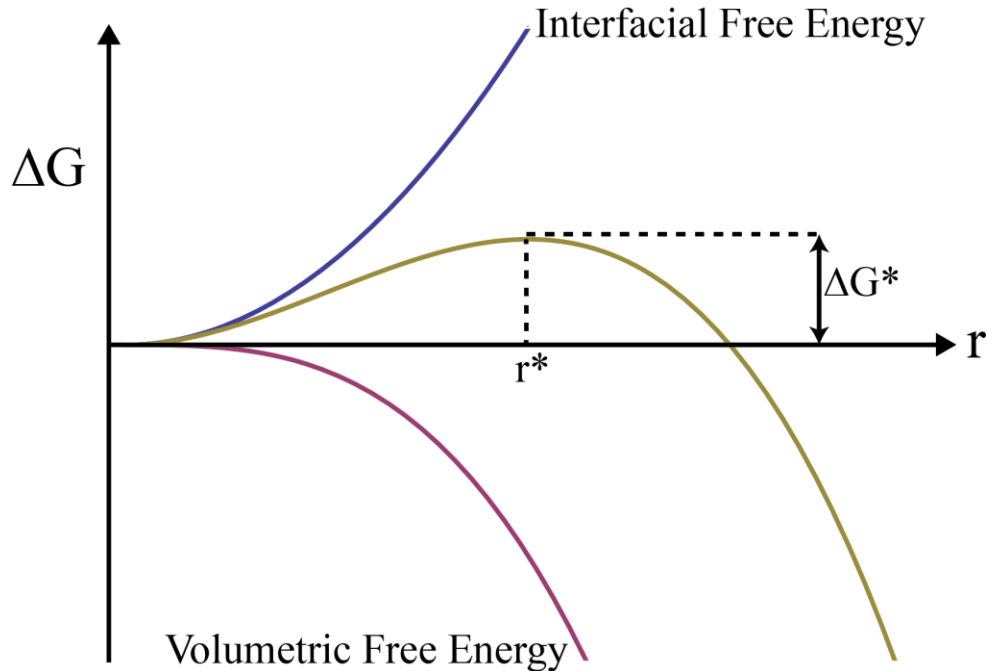


Figure 2.7: Diagram of Gibbs free energy change for nucleation. Curves are shown for the interfacial and volumetric contributions, as well as the combined free energy change, as a function of radius, r . r^* and ΔG^* are the critical nuclei radius and critical free energy change, respectively.

From Figure 2.7 we can see that the critical nuclei radius r^* occurs when the free energy change for condensation is at a maximum. Once the critical radius is reached by a nucleus, the nucleus becomes stable, while those that do not reach the critical radius are subject to dissolution. Referring back to Equation 2.6, it becomes obvious that as temperature increases, the critical nuclei size increases as well.

2.4 - Ostwald Ripening

Once stable nuclei are formed, two stages of thin film growth begin: early-stage cluster growth, and late-stage growth. Early-stage cluster growth can be defined as

2.4 -Ostwald Ripening

the growth of established nuclei while the substrate surface is supersaturated with adatoms, while late-stage growth occurs after supersaturation is lost. Early-stage growth, in the same fashion as nucleation, is driven by a reduction in interfacial energy through condensation [57, 60]. In fact, early stage growth and nucleation usually occur simultaneously. Because established nuclei already have large radii of curvature, and therefore a low surface energy, there is a higher probability of an adatom being added to the established cluster than forming a new nucleus. As a result, clusters continue to grow until the supersaturation of adatoms is lost [62-64].

When enough adatoms have condensed into nanoclusters and the substrate surface is no longer supersaturated, late-stage cluster growth begins. Late-stage cluster growth is best described as the ripening (or growth) of larger clusters at the expense of smaller ones [62, 64]. This process is driven by the Gibbs-Thomson effect, where small clusters become soluble in the equilibrium adatom concentration at high temperatures [65]. This relationship between a cluster's size and its local adatom concentration relative to the equilibrium adatom concentration is shown given by [66, 67]:

$$C_r = C_\infty e^{\frac{2\gamma V_m}{rkT}} \quad (2.8)$$

where C_∞ is the bulk adatom concentration, γ is the surface energy of the cluster, and V_m is the molar volume of the cluster. This equation states that, as cluster radius decreases, the local concentration of adatoms increases. This means that for a system of two particles of different size, there exists a concentration gradient between the two particles that acts as a driving force for mass diffusion from the small to large particle [68]. Figure 2.8 below demonstrates the dissolution of a smaller particle in

2.4 -Ostwald Ripening

proximity to a larger particle—owing to the Gibbs-Thomson effect—as well as a graphical representation of the adatom concentration as a function of distance.

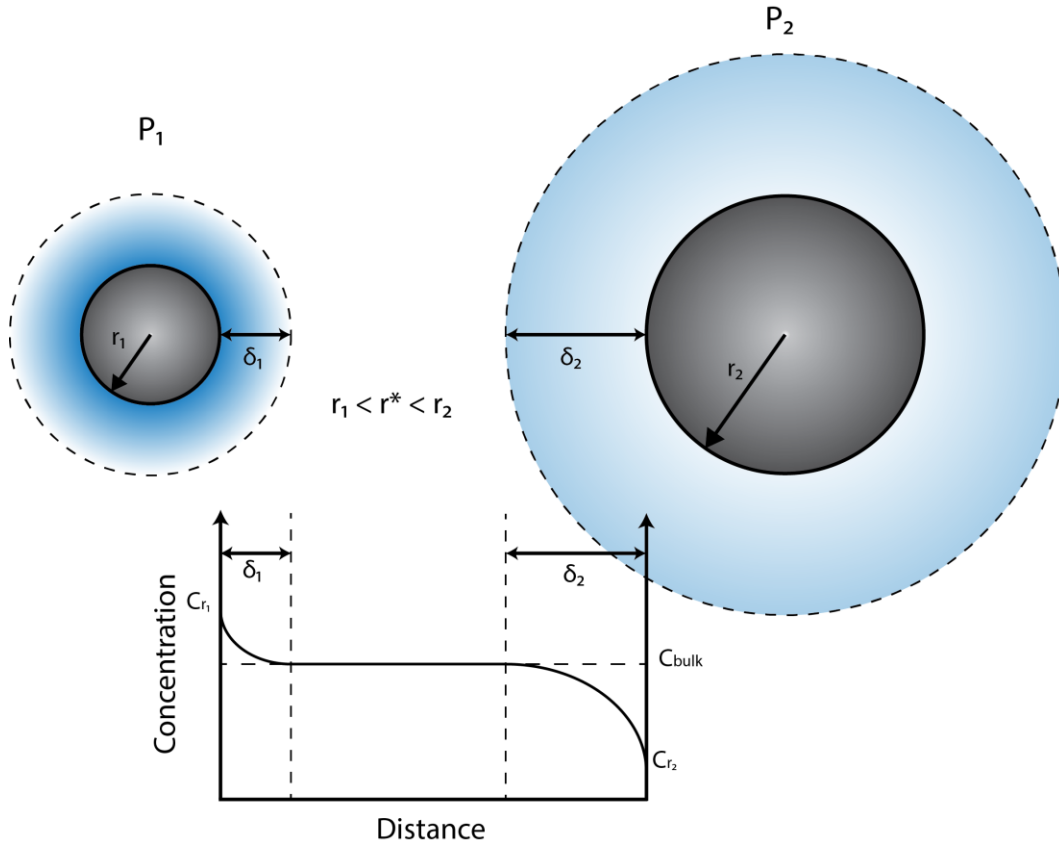


Figure 2.8: Two particle dissolution diagram. The two particles are in close proximity with one another, and C_{bulk} is determined by the average local adatom concentration. δ_1 and δ_2 are diffusion layers formed due to adatoms diffusing faster than they are being incorporated by the particle. C_{r_1} and C_{r_2} are the concentration of adatoms at the surface of P_1 and P_2 , respectively, as determined by the Gibbs-Thomson equation. r^* is the critical particle size at C_{bulk} , meaning that all particles of smaller radius will dissolve, and therefore P_2 will grow at the expense of P_1 .

The first studies on diffusional mass transfer as the facilitating mechanism for Ostwald ripening were performed by Lifshitz and Slyozov [69]. They assumed that all flux to stable clusters was completely absorbed by them, without delay, meaning that the ripening process is controlled entirely by matrix and volumetric diffusion.

Wagner later contributed that due to the time required to form chemical bonds at the

cluster surface, an interface is formed near the clusters where adatoms have built up at a concentration equal to the mean adatom concentration at the substrate surface [67]. While the original size distribution models were formulated for spherical particles in a solid or liquid two-phase matrix, further derivations have been performed for three-dimensional islands on two-dimensional substrates, the system most interesting to us [62, 70-73].

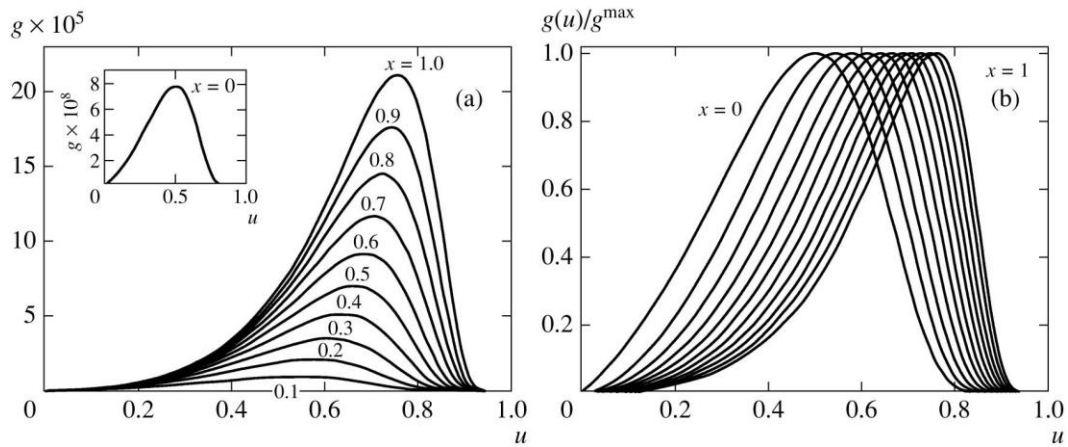


Figure 2.9: Lifshitz-Slyozov Wagner (LSW) size distribution for particles undergoing Ostwald ripening (a), and normalized LSW size distribution (b). u is defined as r/r_g where r_g is the maximum particle size. x denotes the ratio between Wager distributions ($r = 0$) and Lifshitz-Slyozov distribution ($r = 1$), and increases towards $x = 1$ as Ostwald ripening progresses. Figure reproduced with permission from [74].

2.5 - Heat Transfer

To properly design a heating and cooling system for our GLAD deposition system, it is important to understand the fundamentals of heat transfer, as well as the challenges posed by vacuum heat transfer.

2.5 -Heat Transfer

The three modes of heat transfer are conduction, convection, and radiation. All three types of heat transfer facilitate the exchange of energy as a system attempts to reach an equilibrium state.

Heat conduction occurs in solids and is the result of the net movement across a temperature gradient of heat energy carried by electrons and phonons. In metals, heat energy is mostly carried by electrons travelling along metallic bonds, while in other solids, such as oxides, phonons (quantized lattice vibrations) are the primary heat carrier [75]. This difference is due to the high number of free electrons available in metals. The combined contribution from these two heat carriers is defined as the material's thermal conductivity, k ($\text{W m}^{-1} \text{K}^{-1}$), and is related to the rate of heat transfer, q'' (W/m^2) by Fourier's law of heat conduction

$$q''(x) = -k \frac{dT}{dx} \quad (2.10)$$

Convective heat transfer occurs in fluids and is the combined effect of conduction through molecular collisions as well as the bulk flow of matter from areas of high pressure to low pressure. Due to the complex nature of fluid flow, convective heat transfer requires extensive modeling to be predicted.

Surfaces exchange heat energy by emitting and absorbing electromagnetic radiation. The rate at which surfaces exchange heat scales with temperature and is described by the Stephan-Boltzmann law as

$$q = \varepsilon \sigma A (T_s^4 - T_{surr}^4) \quad (2.11)$$

2.5 -Heat Transfer

where ϵ is the emissivity of the surface, σ is the Boltzmann constant, and A and T_s are the area and temperature, respectfully, of the surface, while T_{sur} is the temperature of the surroundings. The Stephan-Boltzmann law tells us that both the surface in question and its surroundings radiatively emit heat, and that the relative temperatures of the two surfaces is what determines the net flow of heat.

When designing a heating and cooling system for an ultra-high vacuum (UHV) system, one must understand the limitations of heat transfer in a vacuum. As previously described, convective heat transfer requires both the conduction of heat through molecular collisions, as well as fluidic mass transfer. Because UHV systems operate in the molecular flow regime, there is insufficient mass available for convective heat transfer at vacuum pressures. This therefore limits our heating and cooling capabilities to conductive and radiative transport modes.

The lack of convective heat transport also leads to a significant decrease in interfacial heat transport rates. When two surfaces are placed in flush contact with each other, the rate of heat transfer across that interface is proportional to the reduction in contact area brought about by surface roughness, as shown in Figure 2.10 below. If contact is not flush, the contact area is further reduced by differences in surface curvature.

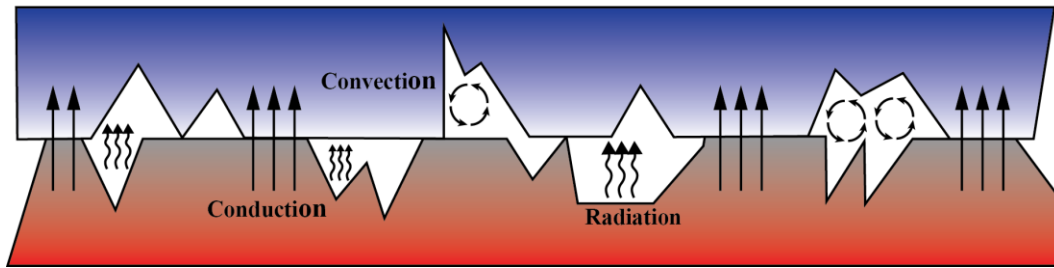


Figure 2.10: Diagram of microscopic interfacial heat transfer. Voids caused by surface roughness between the two surfaces limit the contact area available for heat conduction. Additional heat transfer across the voids is done through a combination of radiation and convection (vacuum conditions limit heat transfer to radiation alone).

Where contact is made, heat transfer occurs conductively, while heat in the void is transferred primarily by convection. Once more, under vacuum conditions, convection effects are negligible, and interfacial heat transfer becomes a function of conduction and radiation.

Chapter 3

Heating and Cooling System Design:

A method of heating and cooling substrates in a controlled manner was required to study the effects of temperature on GLAD film nanostructure. This chapter outlines the process of designing a system for heating and cooling GLAD substrates, including methods for temperature control and temperature measurement. Characterization and calibration of the system is also covered.

3.1 - Introduction

To properly study the effect of substrate temperature on the structure of films grown through glancing angle deposition, we required a heating and cooling system that allowed for accurate measurement and uniform temperature control, while still allowing full rotation about φ and α . The temperature control system must also adhere to the geometrical constraints of the vapour flux, as well as accommodate the lack of convective heat transfer afforded by a UHV environment. Heating, cooling, and temperature measurement each provide unique a challenge to meeting these restrictions, as highlighted below.

Substrate heating can be achieved through either radiative or conductive transfer modes. An issue with conductive heat transfer is the preservation of GLAD motion. Our GLAD system provides rotational motion about φ and α using a series of gears, which are unable to provide significant torsion to the substrate holder to overcome high friction. The rate of heat transfer across a conductive interface is directly proportional to the contact area between the two surfaces, which is also proportional

3.2 -Description of Old System

the force of friction between the two mating surfaces. This trade-off between effective heat conduction and friction thus makes conduction a poor choice for heating. Furthermore, many low-friction greases often contain solvents with high vapour pressures, making them unsuited for use in UHV systems. Therefore, due to this limitation, we must use radiation for heating.

Substrate cooling faces the same interfacial conduction limitation as heating, but with additional complications. Cooling must be done from behind the substrate holder as to avoid the radiative heat from the crucible. Also, radiative cooling would be too inefficient because the available room for a temperature differential between the two surfaces would be limited by absolute zero, as opposed to heating which can come from a heated filament at thousands of degrees.

The difficulties associated with temperature measurement primarily involve where the measurement takes place. For the most representative measurement of the substrate temperature, the measurement device should be in direct contact with the substrate surface. Once more, substrate rotation about φ makes a fixed measurement device difficult. Additionally, the measurement device cannot impede the distribution of flux on the substrate itself.

3.2 - Description of Old System

A previous-generation GLAD heating and cooling system was designed by research group alumnus Martin Kupsta. His design utilized radiative heating from two halogen lamps placed behind the substrate holder. Lamp intensity was controlled manually by adjusting the voltage and current delivered to the lamps through a variable AC autotransformer (Variac). Substrate cooling was accomplished using by

3.2 -Description of Old System

flowing liquid nitrogen (LN_2) through a copper cooling block positioned behind the substrate holder, with copper leaves extending from the cooling block and in direct contact with the substrate holder. A T-type thermocouple in direct contact with a small groove in the back of the substrate holder was used to measure temperature. The thermocouple was connected to a digital millimeter (DMM) together with a thermistor measuring the electrical feedthrough temperature for cold-junction compensation. The voltage readings from the thermocouple and thermistor are entered into a polynomial expression and a temperature is returned. A schematic representation of Kupsta's heating and cooling system is shown in Figure 3.1 below.

3.2 -Description of Old System

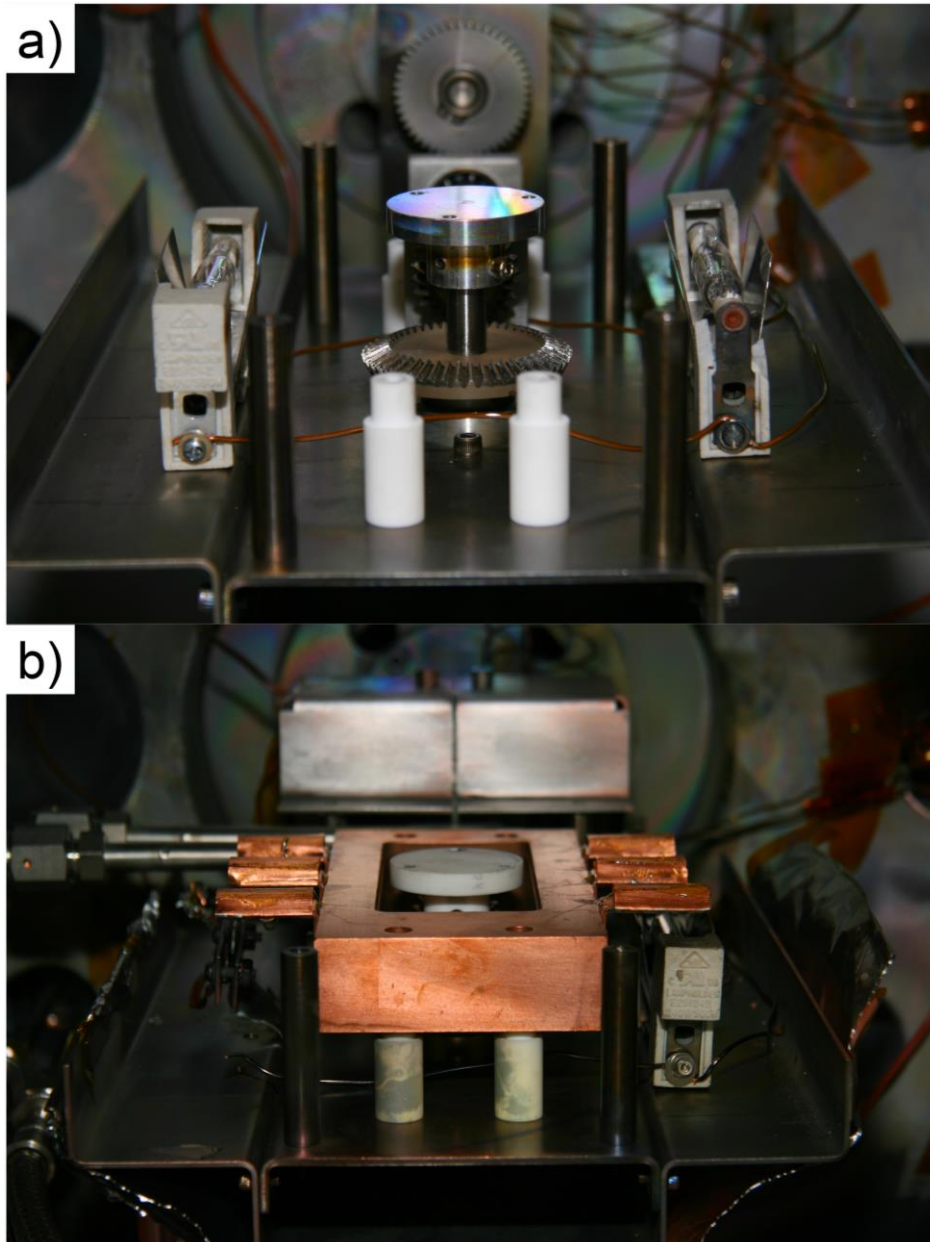


Figure 3.1: Depiction of previous-generation heating and cooling system: a) dual lamp setup located behind the substrate holder, and b) oxygen-free copper cooling block and copper leaves to make direct contact with back of substrate holder.

The system was capable of reaching temperatures as low as $-50\text{ }^{\circ}\text{C}$ using cooling and as high as $400\text{ }^{\circ}\text{C}$ with heating, when measured at the back surface of the substrate holder. Although successful at providing heated and cooled GLAD substrates, this

3.3 -New Heating System

first-generation system had a number of shortcomings that I hoped to improve on. Because the growth front temperature is the parameter of interest, measuring the temperature at the back side of the substrate holder is not representative. Temperature gradients from thermal conduction through the substrate holder and substrate, as well as across the interface between the substrate and holder are the source of this inaccuracy. The conductive cooling path requires as much contact area as possible between the copper leaves and the substrate holder. This contact created enough friction to overpower the ϕ rotation motor, prevented rotation, and required the user to mechanically assist the motor. Finally, placement of the halogen lamps behind the substrate holder created a long response time for temperature change at the growth front, once more due to the long heat conduction path.

3.3 - New Heating System

The primary change made to the heating setup is the location of the lamps. Instead of placing the lamps behind the substrate holder, and requiring a long conductive heat transfer path, the 150 W halogen bulbs were positioned in front of the substrate holder, and directly irradiating the substrate. This change should result in faster response times for changes in temperature, as well as allow for a higher maximum temperature without the loss of heat establishing a temperature gradient through the substrate holder. Lamps were positioned so that they would not block incoming flux at higher α 's, and are attached to the substrate holder arm, allowing them to rotate in α with the substrate, thereby ensuring radiative heating at any α . Aluminum parabolic reflectors were constructed to direct the radiation towards the substrates. Figure 3.2 shows a schematic of the heating lamps and their position once installed in the deposition system.

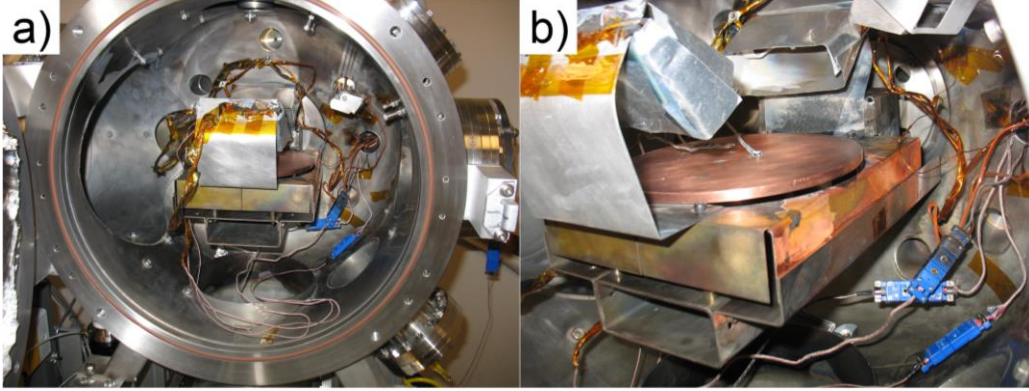


Figure 3.2: New lamp heating system installed in deposition machine. Lamps are positioned in front of the substrate holder and directed at the centre using aluminum parabolic reflectors. The lamps are attached to the housing of the α rotation arm to allow them to rotate with the substrate holder.

3.4 - New Cooling System

A number of cooling options were explored in hopes of providing sufficient cooling to the substrate holder while reducing the friction produced by the previous-generation design. The cooling system should be able to remove heat at a rate equal to or greater than the combined heat of radiation from the source as well as condensation on the substrate holder. The contributions of both radiation and condensation are shown in Equation 3.1, where C_p is the specific heat capacity of the condensing material, H_{vap} is the heat of vaporization, \dot{d} is the deposition rate in (nm/s), ρ is the density of the material, A_{sub} is the area of the substrate, F_{cs} is the view factor between the crucible and substrate, and T_{sub} , T_{cruc} , and T_m are the temperature of the substrate, crucible, and melting temperature of the crucible material, respectively.

$$q = A_{sub}F_{cs}\sigma(T_{sub}^4 - T_{cruc}^4) + \dot{d}A_{sub}\rho_{film}[\Delta H_{vap} + C_p(T_m - T_{sub})] \quad (3.1)$$

3.4 -New Cooling System

The rate of heat addition to the substrate increases with increasing deposition rate, as well as with larger substrates. We imposed further constraints on the system by selecting ZrO_2 as the depositing material, which has the highest melting point of any material ($2715\text{ }^\circ\text{C}$) commonly deposited by our GLAD systems, and therefore will impose the greatest radiative heat flux. Figure 3.3 shows plots of scaling heat flux with increasing substrate size.

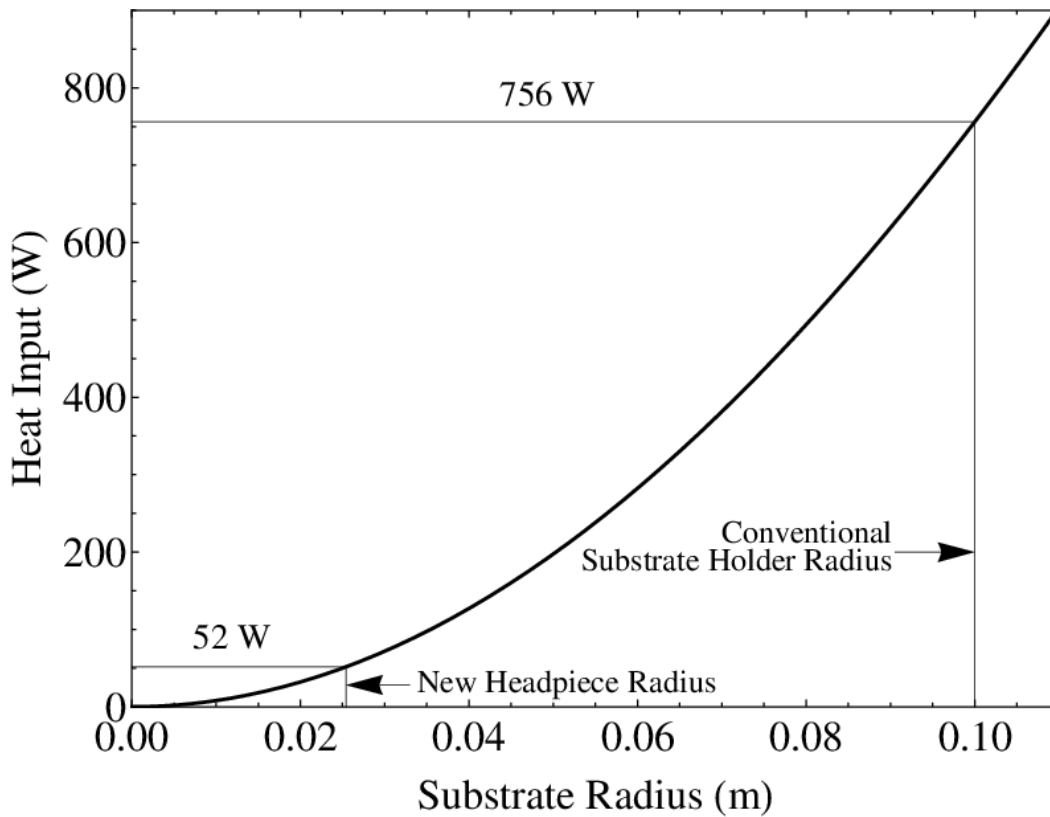


Figure 3.3: Combined radiative and condensative heat input from crucible to the substrate scaling with substrate radius. Assumes a circular substrate in a deposition system with identical geometry to the one for which the temperature control system is being designed. Substrate is positioned at $\alpha = 0^\circ$ to maximize the exposed surface area. The crucible is assumed to be a blackbody point source containing molten ZrO_2 . Calculated heat inputs are indicated for conventional substrate holders and the new headpiece.

3.4 -New Cooling System

Using the curve in Figure 3.3 as selection criteria, several cooling options were explored.

One option examined was using black paint to increase the emissivity of both the cooling block and substrate holder, and then by positioning the two surfaces in as close proximity as possible to each other, have the cooling block radiatively cool the substrate holder. For efficiency and practicality we assumed that the surface area is equal to a disk with an outer radius equal to that of the substrate holder, an inner radius of 5 cm, and the gap between the cooling block and substrate holder is small enough so that the view factor is unity. Using the Stephan-Boltzmann law (Equation 3.1), the surface temperature difference required to radiatively sink the radiation from the source would be greater than the difference between 0 K and room temperature.

With only conductive means for cooling remaining, my focus became on reducing the friction during rotation while preserving the conductive surface area of the copper leaves. Ball bearings may provide a low friction option, but their knife's edge of contact with their housing means poor heat transfer. Due to liquid lubricants being incompatible with our UHV system, I turned to solid lubricants such as graphite or MoS₂. Solid lubricants rely on ultra-low shear forces along specific crystalline planes to provide lubrication, the (001) plane in the case of MoS₂ [76, 77]. These lubricants may operate anywhere in the temperature range where the crystalline phase is stable, which can range from very low -185 °C, to very high 400 °C [78]. Unlike graphite, MoS₂ is able to provide low energy slip planes without being impregnated with water vapour, and is therefore high vacuum-compatible [79].

3.4 -New Cooling System

Copper-impregnated graphite bushings (Graphalloy, 1/2" Inner Dia., 7/8" Outer Dia.) facilitate low friction rotation of the substrate holder, while allowing for sufficient conductive heat transfer. In addition, MoS₂ will be used as a substitute to the graphite as a UHV lubricant.

The Graphalloy bushings were positioned around the shaft of the headpiece to which we connect the substrate holder. This means that the cooling heat conduction path is now through the shaft of the headpiece and into the substrate holder, rather than the backside of the substrate holder. By moving the point of contact to the centre of the shaft, we reduce the lever arm and therefore the torque on the phi motor. Another consequence of moving the conduction path is placing the greatest amount of cooling at the centre of the substrate holder. This changes the temperature distribution at the front surface of the substrate holder so that it is coolest at the centre while becoming increasingly warm at greater radii.

To accommodate the heat flow path through the headpiece, we require a redesigned head piece for increased heat conduction and proper thermal insulation. Oxygen-free copper (OFC) was used to fabricate a new headpiece with a sheath of copper extending down the shaft connecting the headpiece to the rotational gearing. This sheath makes direct contact with the Graphalloy bushings, while the top surface of the bushing makes direct contact with the bottom side of headpiece for additional heat transfer surface area. The phi rotation shaft is insulated from the copper cooling sheath using a 1/32" thick Macor insert. Macor (Corning, Inc.) is a machinable ceramic, which insulates the shaft by adding an additional heat transfer interface coupled with a low heat conduction coefficient. A schematic of the

3.4 -New Cooling System

bushings as well as the OFC headpiece and Macor insert is shown in Figure 3.4 below.



Figure 3.4: OFC headpiece, insulating Macor insert, and Graphalloy bushing used to facilitate heat transfer from the LN₂ cooling block to the substrate holder, while allowing for ϕ rotation. Three set screws are used to secure the headpiece to the rotational shaft.

Improvements were made to the substrate holder for better integration with the cooling through the headpiece. The new substrate holder has a reduced diameter of 4" to reduce large temperature gradients away from the centre, as well as to minimize radiative heat input from the source, as previously demonstrated in Figure 3.3. The reduction in substrate holder diameter decreases the total thermal mass, allowing for faster cooling, but reducing the substrate holder's ability to dampen the heat input from the source. The substrate holder is 1/4" thick, which is twice the thickness of a typical substrate holder, but an inset has been machined so that the headpiece mates with the substrate holder to a depth of 1/8". This should further improve heat conduction, as well as shorten the conduction path. For deposition requiring small

3.4 -New Cooling System

amounts of substrate area, the headpiece itself can be used as a substrate holder, further reducing heat input from the crucible.

We felt that a redesign of the substrate temperature control system should also provide a more representative measurement of growth front temperature, and should therefore measure temperature at the front of the substrate. To achieve this without destroying the film and allowing for rotation, we conceived of a 'dummy' headpiece and substrate holder. Essentially a second bushing/headpiece/substrate holder built into the very same cooling block, in a near similar configuration, but slightly offset from centre and without the ability to rotate. This dummy substrate holder is subject to nearly the same thermal conditions as the actual substrate holder, but allows for a thermocouple to be fastened to the front of a substrate, during deposition.

Schematic drawings of the final cooling block design are shown in Figure 3.5.

3.4 -New Cooling System

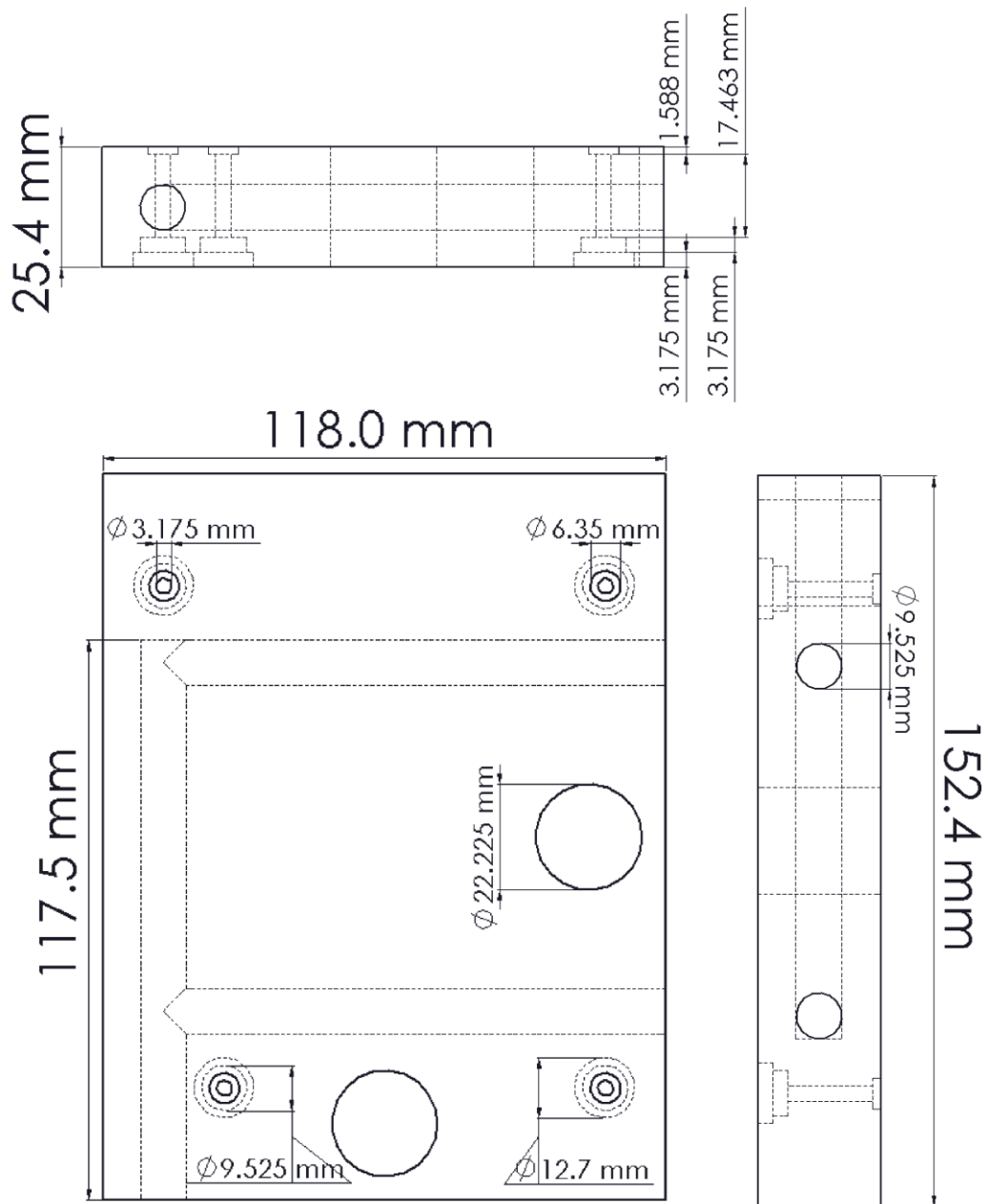


Figure 3.5: Schematic of OFC cooling block. A horseshoe pathway is bored through the interior of the block to provide a pathway to flow LN₂. The LN₂ cools the OFC, which in turn cools the substrate holder through Graphalloy bushings inserted flush into the 22.225 mm dia. holes. Macor standoffs are inserted into the four insets at the bottom side of the cooling block.

3.4 -New Cooling System

The cooling block was fabricated out of oxygen-free copper to ensure maximum thermal conductivity. A U-bend was machined into the cooling block by boring three holes into the copper and then using silver brazing to backfill one of side bores. This U-bend will act as a pathway for the liquid nitrogen. Macor standoffs were fastened to the bottom of the cooling block with screws while mating with insets machined into the copper block. The Macor standoffs thermally insulate the cooling block from the surrounding system. Two 13/16" holes were bored through the cooling block, and then widened until they were 0.002-0.005 in. less than the diameter of the Graphalloy bushings. The discrepancy in diameter between the holes and the bushings is equal to the amount of physical contraction in the bushings during the freeze casting process, so that after reheating, the bushing is compressively held into place. Freeze casting involves cooling the Graphalloy bushings in liquid nitrogen, causing a reduction in diameter allowing the bushings to be placed, then reheating to their original size. The two bored holes are positioned so that they have similar conduction distances from the LN₂ pathway, but far enough away from one another so that the substrate holders will not overlap. The dummy substrate holder needed to be as close as possible to the original substrate holder so that both receive near identical heat flux from the source.

A 1/4" diameter liquid feedthrough from Kurt J. Lesker was installed on the system to deliver LN₂ to the cooling block. To accommodate the rotation about α , our LN₂ delivery system requires a certain degree of flexure. 1/4" convoluted 316L stainless steel core hose with a stainless braid from Swagelok was used to accommodate the flexure required by rotation about α . 316 stainless steel tubes (3/8" dia., 1/16" thickness) were used to deliver the LN₂ from the vacuum feedthrough to the

3.4 -New Cooling System

convoluted hose and then from the hose to the cooling block. The tubes were silver brazed into the cooling block to ensure no leaks would be present in the system. This rigid tubing further reduces the strain on the convoluted hose by limiting its flexure to a single plane. To facilitate this single plane flexure, a stainless steel ‘trumpet’ shaped enclosure was attached to the rotation arm to act as a guide for the convoluted hose. All connections—from feedthrough to tubing to hose—are made with VCR fittings from Swagelok. The VCR fittings employ a knife edge to cut into a metal gasket, forming a vacuum seal. VCR fittings were orbital welded onto the tubing, but came standard on both the feedthrough and convoluted hose. Images of the fully assembled cooling system, installed in the GLAD deposition system, are shown in Figure 3.6 below.

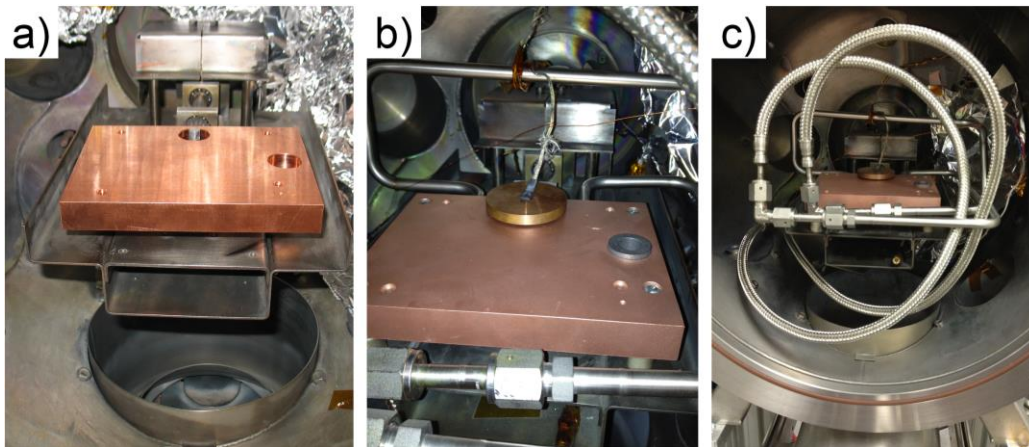


Figure 3.6: a) OFC cooling block installed on the deposition arm. b) Rigid 316 stainless steel tubing secured into the cooling block, complete with VCR fitting welded to the tubing. Graphalloy bushings are visible in the two bored holes, and an OFC headpiece is inserted into the central bushing. c) Convoluted stainless steel hose is fastened to the tubing via VCR fittings.

LN₂ is stored in a large pressurized dewar, while its flow rate into the system is controlled by a simple valve.

3.5 -Temperature Measurement

3.5 - Temperature Measurement

The way which lamp intensity is controlled has also been changed, from a manually-controlled Variac, to an ON/OFF mode solid-state relay run by a PID controller (Omega CNi16). The PID controller receives input from a T-type thermocouple, and varies the ON/OFF duty cycle until the setpoint is reached. A T-type thermocouple was selected due to its vacuum compatibility and accurate temperature measurement between $-200\text{ }^{\circ}\text{C}$ and $350\text{ }^{\circ}\text{C}$ [80]. The CNi16 temperature controller outputs at 10 Vdc and 20 mA to control the 5 A output of a solid state relay to the lamps. Also, by adding a T-type thermocouple feedthrough (Kurt J. Lesker), we were able to eliminate the need for cold junction compensation in the interior of the system. The addition of the temperature controller and thermocouple feedthrough eliminates much of the hassle involved with the old heating setup and allows for the user to focus on controlling other deposition parameters. Figure 3.7 shows a schematic of the temperature controller, alongside a circuit diagram of the connecting thermocouple and lamp power feedthroughs.

3.5 -Temperature Measurement

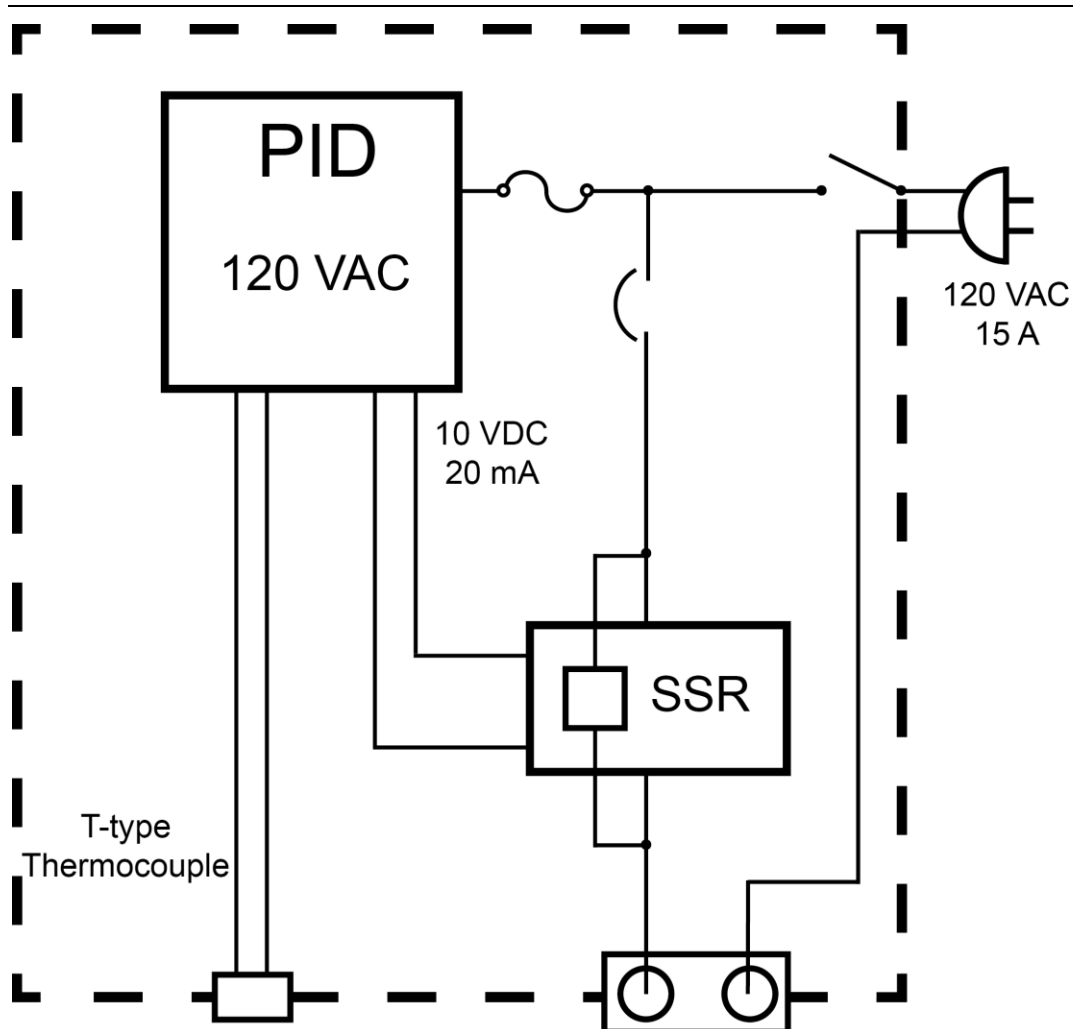


Figure 3.7: Electrical schematic of temperature controller for heating lamps. The PID controller receives input from a T-type thermocouple, and then regulates power to the lamps by way of a SSR.

Initial depositions using the CNi16 controlled heating system revealed an interesting interaction between the lamps and our crystal thickness monitor (Inficon XTC 2 CTM). As the lamps flashed on and off, we observed instabilities in the deposition rate reported by the CTM. When the lamps pulsed off, the reported deposition rate would abruptly increase by $\sim 0.2 \text{ nm s}^{-1}$, then return to the original rate as the lamps pulsed back on. An inspection of how the CTM operates revealed that the temperature of the crystal is an important variable when measuring deposition rate

3.6 -Characterization and Calibration

[81]. According to the CTM documentation, when the crystal crosses a turnaround point temperature (40–80 °C), the measured thickness/rate will decrease. As the lamps are positioned in front of the substrate holder, the CTM is directly illuminated during the on cycle, and an instantaneous decrease in deposition rate is observed. Not only did this make reported deposition rate unreliable, but the variation in reported deposition rate was dependent on the duty cycle of the lamps. The duty cycle required to maintain a set point temperature would become longer at higher temperatures, producing fewer oscillations in measured deposition rate and depositing a thinner film. The simple solution was to place thermal shielding (consisting of a piece of vacuum-compatible aluminum foil) between the lamps and CTM, but with a semi-circle cut out to allow vapour flux to reach the CTM. This re-stabilized the deposition rate measurement, but required the foil shield be adjusted for each α to compensate for the change in geometry.

3.6 - Characterization and Calibration

Proper characterization of the new heating and cooling system—including measurement techniques—was required. Two T-type thermocouples were placed in direct contact with the front surface of a Si substrate; secured using Kapton tape. The Si substrate was fastened to the centre of a 7” diameter oxygen free copper substrate holder, which was then screwed into a macor headpiece. Thermocouple A was connected to the original electrical feedthrough used by Kupsta’s system, while thermocouple B was connected to the T-type thermocouple feedthrough. The temperature controller was hooked up to the thermocouple B to drive the set point. One digital multimeter (DMM) was connected to the electrical feedthrough of thermocouple B, while a second DMM was used to monitor the resistivity of a

3.7 -Chapter Summary

thermistor positioned to measure the temperature of the water cooling line on the CTM.

The temperature controller was programmed to reach set point temperatures starting at 30 °C and increasing to 300 °C in 5 °C increments. Temperature measurements were taken from thermocouple A once the temperature controller reached each set point. As the temperature increased, so did the time required to reach each set point. The PID controller also required more time to maintain an equilibrium temperature, as the duty cycle became longer at higher temperatures. To compensate for this, at set points above 140 °C, the controller was allowed 5–10 minutes to reach an equilibrium temperature before once again selecting a new set point. The substrate holder remained stationary through the duration of the heating. The largest observed difference in measured temperature between the two thermocouples was 2 °C at 35 °C, caused by a slight lag from the temperature controller. The reported difference between the two measurements decreased with increasing temperature, as the controller was able to keep up with the heating rate.

3.7 - Chapter Summary

A vacuum-compatible substrate heating system was designed and constructed. Using a pair of 250 W quartz halogen bulbs to radiatively heat the substrate surface, the system is capable of maintaining temperatures of 300 °C. A T-type thermocouple connected to a PID temperature controller via a thermocouple feedthrough is used to regulate the temperature of the substrate surface.

A redesigned LN₂ cooling system was implemented for *in-situ* substrate cooling. Graphalloy bushings were used to create a low-friction heat conduction pathway to

3.7 -Chapter Summary

an OFC block with LN₂ flowing through it. This system is capable of cooling the front substrate surface to -50 °C, with φ rotation, after 63 minutes of LN₂ flow. Cooling rate is manually regulated through a pressure release valve on the exhaust port.

Chapter 4

Experimental Methodology:

To properly extract quantitative and qualitative information from GLAD thin films, a combination of creativity, precision, and consistency is required. This chapter explains the nuances involved in GLAD depositions and gives an overview of the analytical techniques used in the experiments of Chapters 5 and 6 of this thesis.

4.1 - GLAD Depositions

Some additional preparation is required for GLAD which is not necessary for conventional evaporation deposition. During deposition, control over the rotation in α and ϕ as a function of deposition rate is achieved through a combination of ratio and motion files. The ratio file is material dependent, and reports the relative growth rate at a particular α , when compared to the growth rate of a planar film deposited at low α . The deposition program also includes a built-in tooling factor to account for differences in throw distance and angular distribution of flux between the CTM and the centre of the substrate holder. Motion files are specific to each deposition, and are processed step-wise as a function of film thickness. Each line of the motion file describes a thickness, angle α for that stage to occur at, and angle ϕ to rotate through during the ascribed thickness. Software linearly interpolates between different stages to determine the rotation in α and ϕ . With multiple stages, complex structures may be grown.

4.2 - Wedge chuck

To maximize experimental throughput while preserving experimental control, we designed a substrate holder that allowed simultaneous depositions at different

4.2 -Wedge chuck

incident angles. The substrates were mounted onto an aluminum chuck (shown in Figure 4.1) outfitted with 9 inclined wedges, with faces angled from -20° to 60° (measured from chuck normal vector) in 10° increments.

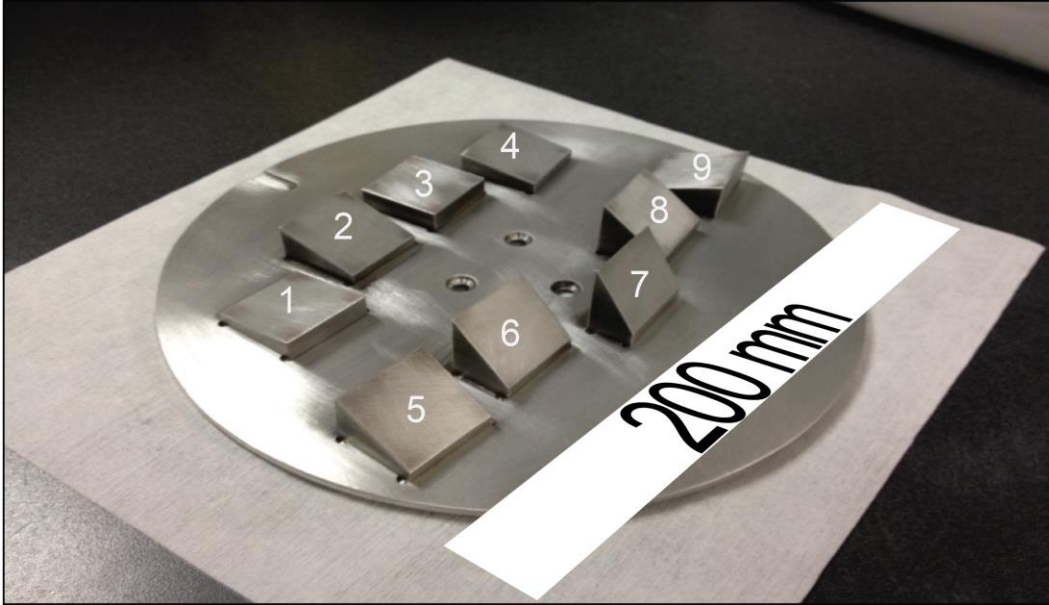


Figure 4.1: Aluminum substrate holder with nine wedge shaped inserts. Each insert provides a surface for substrate mounting with an angle of inclination between 10° and 90° , in 10° increments when the arm is at a nominal $\alpha = 30^\circ$. Table 4.1 further outlines the various parameters of each wedge position.

The wedges have different cross sectional areas with respect to the evaporation source and the heating lamps, and different footprints on the aluminum chuck. These differences modify the thermal conditions for each wedge during deposition. As a result, it was necessary to calibrate each wedge temperature relative to a nominal temperature. The nominal temperature is reported by the Type-T thermocouple secured on top of a bare piece of Si wafer ~ 4 cm from the center of the aluminum chuck. The substrate temperature on each wedge was measured as a function of nominal temperature; the parameterized relationship is shown in Table 4.1.

4.3 -Image Preparation

Table 4.1: Deposition parameters for respective wedge chuck positions.

| α | Relative Dep Rate | Temperature at: | | | | |
|----------|----------------------|-----------------|--------|--------|--------|--------|
| | | 100 °C | 150 °C | 200 °C | 250 °C | 300 °C |
| 10 | 0.85 | 55 | 107 | 161 | 215 | 268 |
| 20 | 1.18 | 32 | 77 | 127 | 172 | 213 |
| 30 | 1.14 | 37 | 76 | 112 | 154 | 203 |
| 40 | 0.96 | 56 | 112 | 168 | 225 | 275 |
| 50 | 0.84 | 35 | 76 | 110 | 153 | 196 |
| 60 | 0.44 | 34 | 71 | 110 | 151 | 193 |
| 70 | 0.35 | 29 | 54 | 89 | 130 | 178 |
| 80 | 0.18 | 19 | 48 | 83 | 106 | 153 |

The temperature of each wedge position increases linearly with nominal temperature, but at uneven rates. As a result, higher nominal temperatures will lead to a greater temperature divergence.

Non-uniformity in GLAD thickness due to the angular distribution of vapour flux has been well characterized by Wakefield and Sit [82]. The wedges protrude from the substrate holder in the normal direction providing additional non-uniformity compared to a regular chuck. Using Wakefield's formulism for calculating flux distribution, deposition rate for each position was calculated relative to the centre of the chuck and tabulated in Table 4.1. All calculations were made for the wedge chuck angled at a nominal $\alpha = 30^\circ$. I have included the expected relative deposition rates normally produced by the respective wedge chuck deposition angles, for comparison. It is important to note the deviation from the expected deposition ratios brought about by the wedge geometries.

4.3 - Image Preparation

Once we have obtained SEM images of our samples, computational image analysis is necessary to extract statistical size and separation data. For hemispherical cap shaped seeds and GLAD posts, plan-view cross-sectional area is the measured size

4.3 -Image Preparation

parameter, while centre-to-centre distance is measured for separation data. While some software packages are able to process greyscale images, ImageJ requires that the SEM micrographs be converted to a binary (black and white) image. This step requires us to select the range of greyscale values (0:255) that represent objects in the foreground, so that we may differentiate them from the background.

This thresholding step was carried out in Wolfram Mathematica through the `MinDetect[image, h]` function, where `h` is percentage of normalized pixel values ranging from 0 to 1. This function begins by selecting pixels with the lowest greyscale values, then assesses if the nearest neighbour pixels fall within the pixel value range specified by `h`. The function continues this assessment for all connecting pixels until a map of extended minima is created, which is then returned by the `MinDetect` function as a binary image. An additional function is then used to fill in thresholded elements whose centres were outside of the pixel value range, `h`.

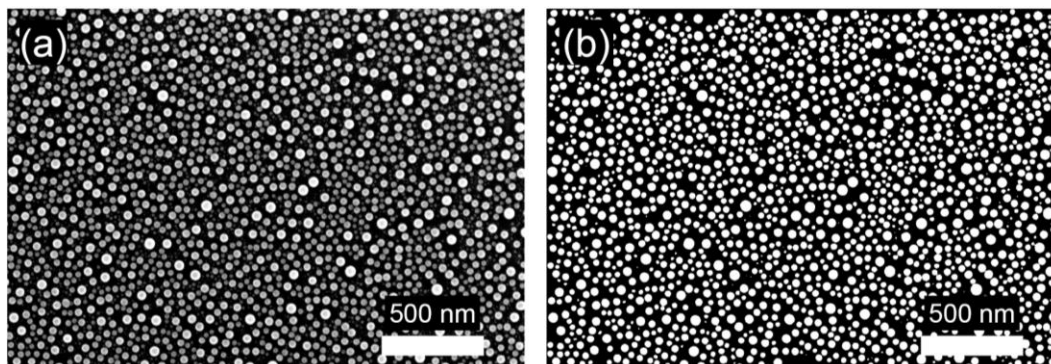


Figure 4.2: (a) Sn seed layer deposited at 300 °C to a thickness of 4.7 nm. (b) Same film as (a), but after binarization and segmentation has been performed.

Segmentation of thresholded images is necessary to isolate individual posts and seeds, preventing the analysis of a multicomponent structure as a single element.

4.4 -Image Data Analysis

Segmentation begins by using the product of the thresholding step as a ‘marker’, indicating which pixels on the original image are to be converted to the foreground of a new binary image. The foreground region specified by the marker is then extended outwards by a specified pixel distance. To avoid measuring only part of an element cut off by the edge of the image, all foreground regions extended to the image edge are removed. A watershed function is then used to segment individual elements, using a marker of minimum pixel value locations to specify where to begin the flooding. A border is drawn where two basins meet, segmenting the two elements.

4.4 - Image Data Analysis

Size analysis was performed using ImageJ’s built in particle analysis tool, Analyze Particles. Analyze Particles scans the image until the edge of an object is reached, at which point it outlines the object, measures its area, then renders it invisible, and continues scanning for new objects. Particles may be excluded by setting a threshold limit on size and circularity, where circularity = $4\pi/\text{Perimeter}^2$, and ranges from 1.0 (a perfect circle) to 0.0 (infinitely elongated). Size data is reported on a per-particle basis which can then be used to generate a size distribution histogram. Figure 3.3 displays a segmented SEM image of Sn nanoclusters and its corresponding map of outlined particles after the particle analysis has been run.

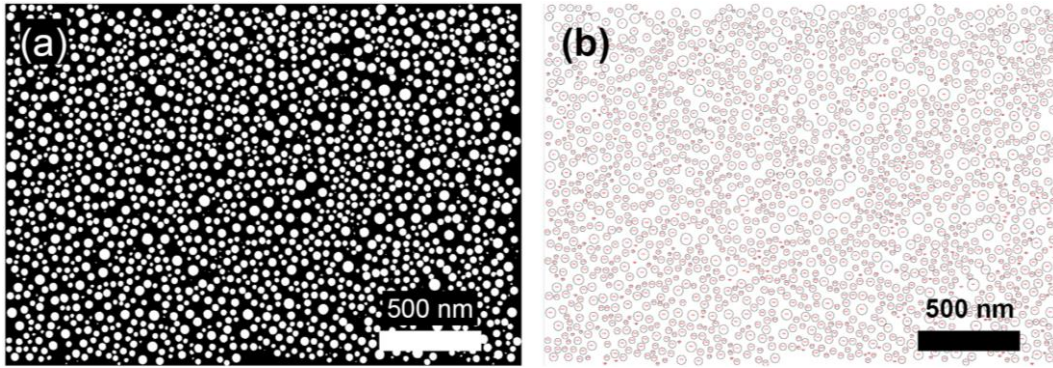


Figure 4.3: (a) Binarized and segmented image of Sn seed layer grown at 300 °C to a thickness of 4.7 nm. (b) Measurement map of outlined particles, from which area data is obtained.

To quantify possible effects on the short- or long-range order of our films, we turned to spatial autocorrelation analysis. Spatial autocorrelation determines the degree to which a weighted quantity in a 2D plane is cross-correlated with itself. That is to say, spatial autocorrelation may determine whether or not ordering occurs in a seemingly stochastic process, as well as the degree of ordering [83]. The autocorrelation process will determine if there is a spatial dependency of any element on the plane on any other element. These dependencies may include element separation, shared directionality, or even long range ordering of elements. Autocorrelation was performed on unsegmented plan-view SEM images using a Mathematica software package (developed by Joshua Laforge). The software package finds the centre-to-centre distances for each element in the SEM image, and then plots the frequency distribution of separation distances, normalized by the mean frequency.

4.5 - Chapter Summary

GLAD depositions use complex motion algorithms to control the rotations in α and φ , and facilitate the growth of different structures. A custom substrate holder was

used to provide deposition at nine different α , in parallel, from 10–90°, in 10° increments. This increased our experimental throughput nine-fold.

The physical properties studied in Chapters 5 and 6 are extracted through inspection of SEM images. To ensure precision and preserve consistency, we turned to automated digital image analysis algorithms. These algorithms first prepare the images for analysis by thresholding, binarization, and segmentation, then extract the desired physical quantity from prepared image.

Chapter 5

Effect of Temperature on β :

This chapter probes the effects of increased substrate temperature on column tilt angle β for slanted post films grown from various materials. I compare β for Al, Cu, Si, Ti, and TiO₂ when deposited at room temperature and at elevated substrate temperature. β is measured from cross sectional SEM images with ImageJ computer software. This work was done in collaboration with Dr. Michael Taschuk, research associate, and Joshua LaForge, Ph.D. student, from Prof. Michael Brett's research group.

5.1 - Introduction

Structured films grown through GLAD typically exhibit a number of quantifiable physical characteristics, such as column tilt angle or helical pitch, and are referred to as growth parameters. By controlling the physical and geometrical conditions of each deposition—also known as deposition parameters—we may produce films with specific growth parameters. Unfortunately, many of these deposition parameters are coupled to several growth parameters, limiting our control to larger subsets of physical characteristics. One parameter of interest, β , has been readily modified by changing the angle of inclination [84]. Unfortunately, as a is increased, column spacing also increases, and rapidly at $a > 80^\circ$.

As previously covered in Chapter 1, β has been experimentally observed to be a function of substrate temperature. With the control over substrate temperature offered by the new heating system, we hope to show the ability to change β with

5.2 -Experimental Setup

temperature for multiple materials. This adds additional dimensionality to the deposition program, hopefully decoupling growth parameters normally associated with β .

Lichter and Chen quantified the effect of temperature, together with surface roughness and deposition angle, on β , in the form of Equation 5.1:

$$\tan \beta = \frac{2}{3} \tan \alpha / \left(1 + \frac{4}{27} h_1 J / D \tan \alpha \sin \alpha \right) \quad (5.1)$$

where h_1 is the average substrate roughness, J is deposition rate, and D is the diffusivity of the adatom species, previously described by Equation 2.3. Because diffusivity increases with temperature, β is predicted to decrease with hotter substrates, which was experimentally observed by Nakhodkin *et al.* [23].

In this chapter, I investigate the effects of elevated substrate temperature during deposition on the column inclination angle grown by metals, semiconductors and oxides, each with a different melting temperature. Cross-sectional SEM images are used to identify changes in structure, which are compared with results from the literature.

5.2 - Experimental Setup

Ti, Al, Cu, Si, and TiO₂ were selected as deposition materials because of their wide range of melting temperatures, as well as to distinguish between possible mechanistic differences in metals, oxides, and semiconductors. Important properties of these materials are found in Table 5.1 below.

5.2 -Experimental Setup

Table 5.1: Relevant properties of various material used for slanted post deposition.

| Material | Material Type | T (K) | Substrate T (K) | T/T_m |
|------------------|---------------|---------|-------------------|---------|
| Al | Metal | 933 | 573 | 0.61 |
| Cu | Metal | 1358 | 573 | 0.42 |
| Si | Semiconductor | 1687 | 573 | 0.34 |
| Ti | Metal | 1941 | 573 | 0.30 |
| TiO ₂ | Oxide | 2116 | 423 | 0.20 |

Slanted post deposition was performed in a high vacuum (base pressure < 0.13 mPa (< 1 μ Torr)) chamber using an electron beam evaporation system (Kurt J. Lesker AXXIS). Evaporant materials used were: Ti (6 mm pellets, 99.8% purity, Cerac), Cu (6 mm pellets, 99.99% purity, Advanced Materials), Al (120–130 mg slugs, 99.99% purity, Kurt J. Lesker), Si (3–6 mm pieces, 99.999% purity, Kurt J. Lesker), and TiO₂ [3–6 mm pieces, 99.9% purity, Cerac]. Source materials were evaporated from graphite crucibles (except for Si for which we used a Cu crucible) at a nominal deposition rate of 1 nm s^{-1} (0.1 nm s^{-1} for Si), measured by a CTM. Slanted posts were deposited on Si wafers (4" diameter, $<100>$, p -type, test grade from University Wafer), cleaned prior to deposition with isopropyl alcohol followed by de-ionized water and then blown dry with N₂ gas. Substrates were mounted to the wedge chuck as described in Section 4.2, which when tilted to a nominal angle of incidence of 30° , produce 10 deposition angles 10 – 90° in 10° increments. A T -type thermocouple was placed in direct contact with a Si substrate, taped to the centre of the wedge chuck.

Prior to deposition, substrates were heated to nominal temperatures of 150 °C for TiO₂, and 300 °C Ti, Cu, Al and Si depositions. During substrate heating, depositions began immediately once the temperature set points were reached and heating was terminated immediately after films reached the desired nominal

5.3 -Experimental Results

thicknesses of 500 nm. Vacuum conditions were maintained until the substrate temperature had fallen back to 40 °C.

As-deposited slanted post films were cleaved parallel to the flux direction and mounted with Ag paint into stainless steel SEM sample holders. Special attention was made while mounting the substrates to the wedge chuck so that the substrate edge was in line with the flux direction. A scanning electron microscope (SEM, JEOL 6301F) was used to capture images of slanted post films.

Column tilt angle was measured from SEM images using a built-in angle measurement tool in ImageJ. Lines were drawn manually down the post directions, while an additional line was drawn along the substrate plane. The angle formed between the post growth direction and the substrate plane forms the complementary angle to the column tilt angle. Special care was put towards only selecting clear and distinct posts for measurement. In addition, measurements were taken from both extinct posts and posts which grew to the full thickness of the film. A minimum of 12 measurements were captured for each image, with two images per sample. For each film, a histogram of β measurements was plotted, and a Gaussian distribution was fit to the data. The mean and standard deviation of each Gaussian was extracted by the fit routine.

5.3 - Experimental Results

Figure 5.1 shows plan view SEM images of Ti, Cu, Al, Si, and TiO₂ slanted post films grown at both room temperature and at elevated substrate temperatures.

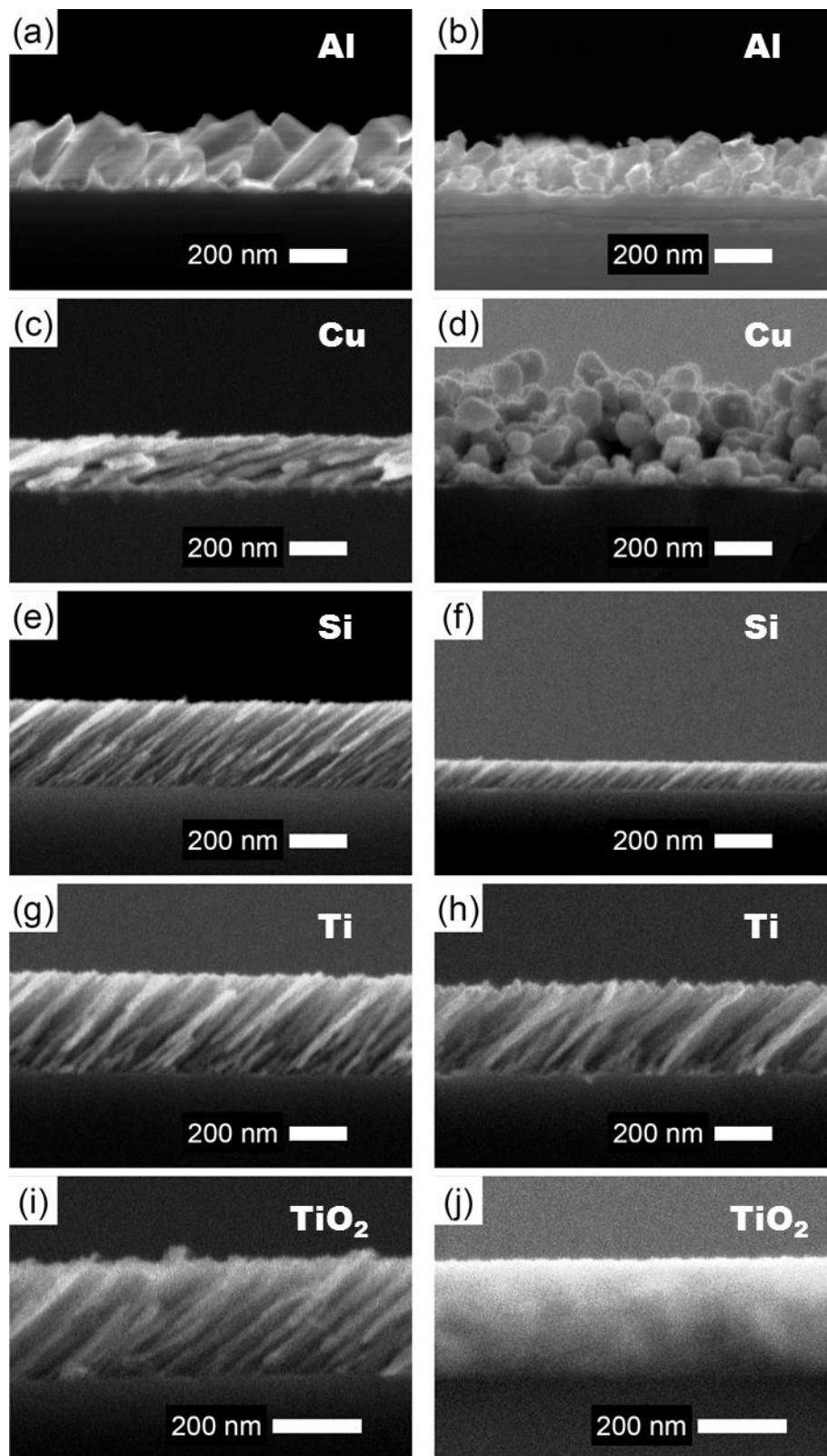


Figure 5.1: SEM images of 500 nm thick ((f) 200 nm thick) slanted post films grown at room temperature (Left), 300 °C (b), (d), (f), and (h), and 150 °C (j). All films grown with an angle of incidence $\alpha = 80^\circ$.

5.3 -Experimental Results

Slanted post TiO₂ films grown at 150 °C and Cu films grown at 300 °C appear highly dense, to the point where little to no columnar structure was observed. Even when deposited at room temperature, TiO₂ and Cu films grown at $a = 60^\circ$ do not exhibit a structure defined well enough from which to make appropriate β measurements. Al slanted posts grown at room temperature and at an incidence angle of 80° resemble broad columnar structures. The columns have an observable inclination angle in the direction of flux, but their asymmetrical shape makes determining this angle difficult with any degree of accuracy or consistency. Al films grown at 80° and on substrates at 300 °C appear as irregularly shaped posts, without discernable growth direction with respect to incidence angle. For these reasons, we shifted our focus towards the Si and Ti slanted post films.

Column inclination angle measured from Si slanted posts ($a = 80^\circ$) were found to be $(51.0 \pm 1.3)^\circ$ and $(50.2 \pm 1.8)^\circ$ when deposited on substrates at room temperature and 300 °C, respectively. The ratio of measured film thickness to nominal film thickness was found to be 0.61 and 0.52 for slanted post films grown on substrates at room temperature and 300 °C respectively.

Figure 5.2 shows average measured β for Ti slanted post films grown at various angles of incidence, grown on substrates at both room temperature and 300 °C.

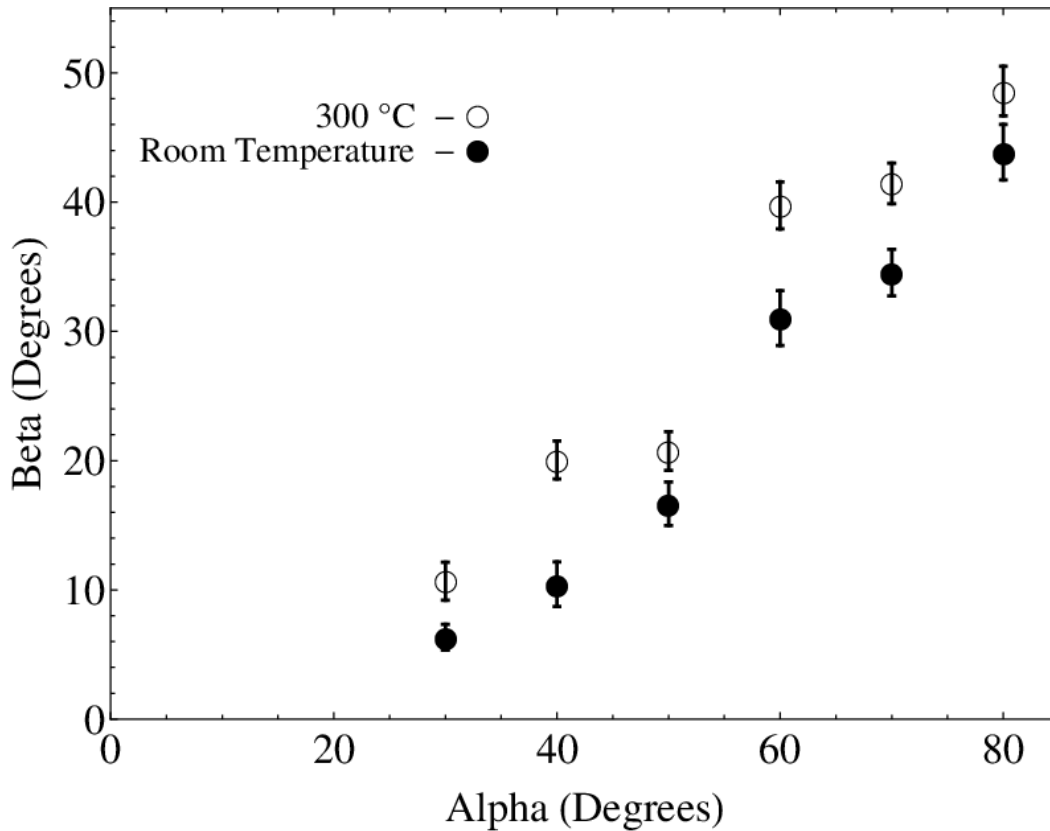


Figure 5.2: Angle of incident flux and the measured column tilt angle of Ti slanted posts deposited at room temperature and 300 °C. Error bars represent one standard deviation from the mean.

Ti slanted posts increased an average of $6.4^{\circ} \pm 2.2^{\circ}$ when deposited on substrates at 300 °C, compared to substrates at room temperature. Error is reported to one standard deviation.

5.4 - Discussion

Deposition at elevated substrate temperature resulted in loss of the discernable slanted post structure for Al, Cu, and TiO_2 . For Cu and Al, this loss is attributed to an increase in adatom mobility, to the point where adatoms are able to diffuse greater distances than intercolumn spacings, effectively leaving the ballistic growth regime. A substrate temperature of 300 °C equates to a T/T_m of 0.42 and 0.61 for Cu and Al

respectively, both beyond the theoretical columnar Zone 1 limit of $T/T_m = 0.3$ [1]. The erratic structure observed in the Al film may be compared to similarly unstable Ag structures grown by Khare *et al.* at elevated temperature [85]. Crystalline nanowires with high aspect ratios formed due to an excessive increase in adatom diffusion length. The TiO_2 deposited at a substrate temperature of 150 °C has a T/T_m of 0.2, which should remain in Zone I. Furthermore, Deniz *et al.* propose that, due to differences in diffusion rates among metal and oxygen adatoms, metal oxides have a higher threshold temperature for forming GLAD structures, with T/T_m ratios of approximately 0.5 [86]. This suggests that other mechanisms may be responsible for the loss of structure observed in the TiO_2 films deposited at elevated temperature.

As expected, Ti column inclination angle increased with increasing α , as predicted by both the tangent rule and the work done by Tait [18-20]. The increase in β with temperature in Ti contradicts what is predicted by Lichter *et al.* as well as what was experimentally observed by Nakhodkin *et al.* [22-23]. Instead, the increase in β with increased substrate temperature could be more closely compared to results obtained by Sorge *et al.*, where increasing ion bombardment also lead to an increase in column inclination angle [27]. The heat energy imparted on the film during ion bombardment could replicate similar heating conditions as with our experiments, resulting in a similar effect on β as we observed. As to why increased substrate temperature would result in an increased column inclination angle, it is difficult to say. One would expect an increased substrate temperature would lead to increased adatom mobility, which, due to the isotropy of adatom hopping, would decrease the influence of flux directionality on the structure of the film. Instead, we found that

5.5 -Chapter Summary

increased substrate temperature lead to the formation of column inclination angles closer to the angle of flux incidence. This departure from the literature was found consistent with repeated experiments, but because of the limited dataset, further conclusions cannot be made.

Patzig *et al.* studied the effect of increasing substrate temperature on the structure of helical and vertical post Si films grown through glancing angle deposition [87]. They found that as substrate temperature was increased, helical post film height also decreased. They also observed an initial increase in helical definition with increasing temperature, but found that further increase in temperature lead to columns merging together and a loss of structure. Patzig *et al.* argued that increased substrate temperatures lead to an increase in adatom diffusion distance, down the length of the columns providing a more consistent column diameter throughout. At even higher substrate temperatures, they suggest that adatom diffusion increases to the point where intercolumn hopping occurs, and posts begin to merge prematurely. Based on results obtained by Patzig *et al.*, I expected a change in Si column inclination angle with increased substrate temperature. Instead, the column inclination angle remained unchanged at 300 °C. While column inclination angle remained constant with increased substrate temperature, the ratio of measured thickness to nominal thickness decreased from 0.61 to 0.52. This indicates a densification of the film with increasing substrate temperature; consistent with the findings by Patzig *et al.*

5.5 - Chapter Summary

This chapter provides insight into the complexity of the slanted post growth process. The structure and column inclination angle of slanted posts grown from Al, Cu, Si, Ti, and TiO₂, behaved in a different way when substrate temperature was increased.

5.5 -Chapter Summary

Al and Cu, metals with low melting temperatures, lost discernable columnar structure at elevated substrate temperatures. Si slanted posts remained unchanged at elevated substrate temperatures; while Ti slanted posts demonstrated an increase in β with increasing substrate temperature, even though the two materials have comparable melting temperatures. TiO_2 , although having the highest melting point of all materials studied, formed a dense film at elevated substrate temperature. It becomes clear that we cannot establish a single relationship to govern the interaction between substrate temperature and β .

Chapter 6

GLAD Nucleation:

This chapter describes a low-cost method for producing seed layers for GLAD films. Digital image analysis is used to extract size distributions and average separation distance data for Sn seed layers deposited at a range of substrate temperatures, and grown to different thicknesses. SiO₂ vertical posts are deposited onto these Sn seed layers, and the change in post separation distance is measured and quantified through similar methods. This work was done in collaboration with Dr. Michael Taschuk, research associate, and Joshua LaForge, Ph.D. student, from Prof. Michael Brett's research group.

6.1 - Introduction

The self-shadowing growth mechanism that initiates columnar growth also prevents further nucleation since the substrate becomes completely shadowed. Therefore, the initial nuclei act as a template for the GLAD film. If we can control nuclei location, then we can control position of GLAD posts grown on top of the established nuclei.

Various methods have been explored to fabricate seed layers including electron beam lithography (EBL) [88-90], nanoimprint lithography (NIL) [91], colloidal self-assembly [92-93] and self-assembled block copolymers [94].

Seeding a GLAD film is a tradeoff between precision and cost. The ultimate in precision is achieved with e-beam lithography, which allows extremely precise seed placement, including the possibility of engineered defects or channels. However, the high cost and limited substrate area that can be patterned restricts this method to

6.2 -Experimental Setup

those cases such as photonic crystals where the best possible control is absolutely required. Nanoimprint lithography uses EBL as an initial step, but then replicates the pattern across larger areas, reducing the cost but at the risk of introducing stitching artifacts. Further reductions in cost can be achieved using colloidal aggregates or block co-polymers, but the long range order may be poor. Moreover, the available seed spacing and geometry can be somewhat restricted.

One common feature of the seeding methods used to date has been the requirement for pre-deposition substrate preparation. In this chapter, I investigate a low-cost seeding method which can be used *in situ* before a GLAD deposition. Without a vacuum break, we deposit a nucleation layer using a material which forms distinct nuclei as well as demonstrate high adatom mobility. Using controlled substrate temperature, we demonstrate tuneable seed layers for GLAD. We will then switch to a more traditional GLAD material to deposit our columnar structures, which will inherit the substrate positions of the already deposited seed layer.

6.2 - Experimental Setup

Seed fabrication was performed in a high vacuum (base pressure < 0.13 mPa (< 1 μ Torr)) chamber using an electron beam evaporation system (Kurt J. Lesker AXXIS). The chamber was outfitted with a custom motion feedthrough capable of controlling vapour incidence angle, α , while providing substrate rotation normal to the substrate holder, about the angle ϕ . Sn pellets (3 mm, 99.9% purity, Cerac, Inc.) were evaporated from a graphite crucible at a nominal deposition rate of 0.1 nm s^{-1} and a source – substrate distance of 43 cm. Nominal deposition rate is measured by

6.2 -Experimental Setup

a quartz crystal monitor (QCM), which provides feedback to the motion control software. The Sn seeds were grown on Si wafers (4" diameter, <100>, p-type, test grade University Wafer). Prior to deposition, substrates were cleaned using an isopropyl alcohol wash, then rinsed with deionized water, and finally air-washed with dry N₂ gas. This procedure was repeated with Cu (6 mm pellets, 99.99% purity, Advanced Materials) and Al (120–130 mg slugs, 99.99% purity, Kurt J. Lesker) under similar vacuum conditions and at an identical nominal deposition rate.

Substrates were heated prior to deposition using a pair of 250 W quartz halogen bulbs (Philips, 79 mm). To increase heating efficiency, we used a pair of custom aluminum parabolic reflectors to direct more black body radiation towards the chuck's surface. Bulb power was regulated by a temperature controller (Omega CNi16) in a PID-regulated ON-OFF mode, using a T-type thermocouple for feedback. The use of pulsed ON-OFF modulation for the bulbs required shielding the QCM from the heating lamps with aluminum foil. Otherwise, the QCM housing temperature changed in response to the lamp state, inducing changes in the measured deposition rate, interfering with the feedback for the α and ϕ stepper motors.

Seed layers (nominal thickness 4 nm at the chuck's center when $\alpha = 30^\circ$) were deposited at nominal temperatures of 150 °C, 200 °C, 250 °C and 300 °C. Deposition started once the temperature setpoint was reached, and heating was terminated the moment the desired thickness was reached. The deposition system remained at high vacuum until the nominal temperature dropped below 60 °C, at which point the system was vented with dry-N₂ purge gas and opened to atmosphere.

6.2 -Experimental Setup

Silicon dioxide vertical posts with 50 nm, 100 nm, 200 nm, 500 nm, and 1000 nm thicknesses were grown on the seeded substrates by rotating the chuck, during deposition, about φ , completing one full rotation for every 20 nm of growth, while being held at a constant $\alpha = 85^\circ$. Growth of silicon dioxide vertical posts took place in the same high vacuum (base pressure < 0.13 mPa (< 1 μ Torr)) chamber described above, using an electron beam to evaporate SiO₂ (1–3 mm pieces, 99.99% purity, Cerac) at a nominal deposition rate of 1 nm s⁻¹.

A scanning electron microscope (SEM, Hitachi S-4800) was used to image the seeds and vertical posts samples. A Mathematica (Wolfram Research) image processing package was used to prepare images for automated particle size analysis using ImageJ software. Size distributions were extracted from five different images for each seeded substrate. By fitting a Gaussian to the size distribution from each image, a mean diameter and standard deviation was found for Sn seeds grown at all five temperatures.

To study the effect of Sn seeds on SiO₂ vertical posts, an autocorrelation function was used to determine the average nearest-neighbour distance for each seed. This autocorrelation measurement was repeated for SEM micrographs of SiO₂ vertical posts grown on top of the Sn seed films, and the average separation distance of each vertical post was extracted, to be compared with the average separation distance of the corresponding Sn seeded film. Before applying the autocorrelation function to our films, we tested its accuracy for measuring average separation distance on an image with particles with known separation distances. For this purpose, a SEM image of a hexagonal close packed monolayer of nickel nanoparticles was selected,

6.2 -Experimental Setup

with easily measured separation distance [95]. Centre-to-centre distances were measured to 5 connecting nearest neighbours for 3 different particles, from which I found a mean separation distance of 14.9 pixels. The SEM image is shown together with the autocorrelation output in Figure 6.1.

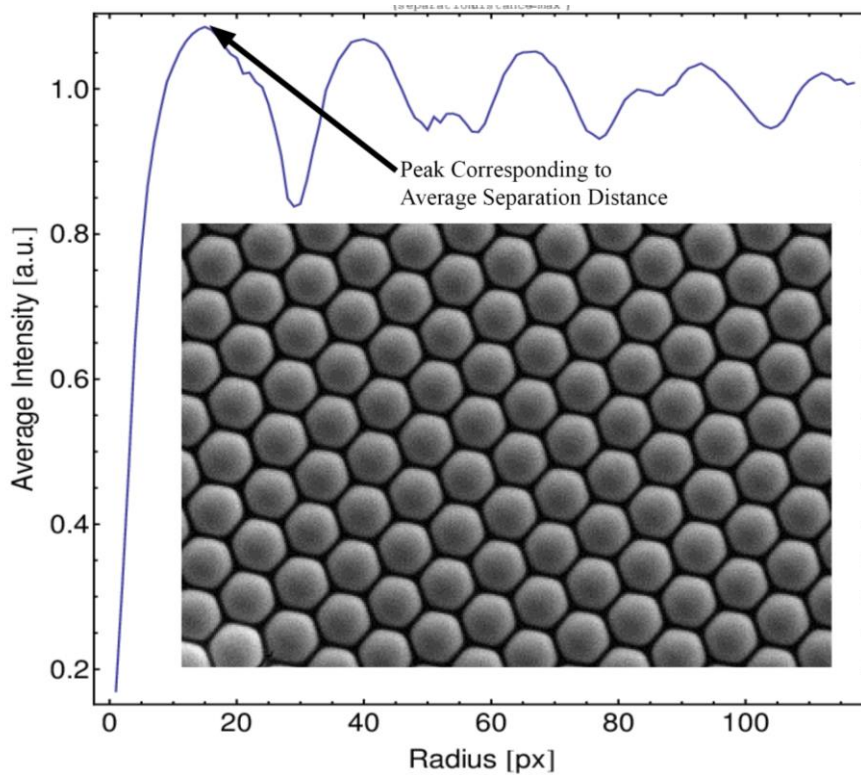


Figure 6.1: Autocorrelation of a hexagonal close packed nickel nanoparticle monolayer. First peak represents average separation distance. Periodic peaks represent periodicity in centre to centre distances generated by the HCP structure. Image adapted with permission from [95].

The distribution of correlation distances in Figure 6.1 show a periodicity expected of the HCP lattice, with the first peak corresponding to the centre to centre distance of nearest neighbours. The location of the peak was found to be 14.87 pixels, using a parabolic curve fit, in full agreement with manual measurements.

6.3 - Experimental Results

Plane-view SEM images of Al, Cu, and Sn seeds grown at different temperatures are shown in Figure 6.2. The seed layer formed by Al and Cu was unsatisfactory due to their closely spaced, irregular shapes. On the other hand, Sn seeds formed distinct, well-separated seeds at relatively low temperatures, and were selected for further investigations.

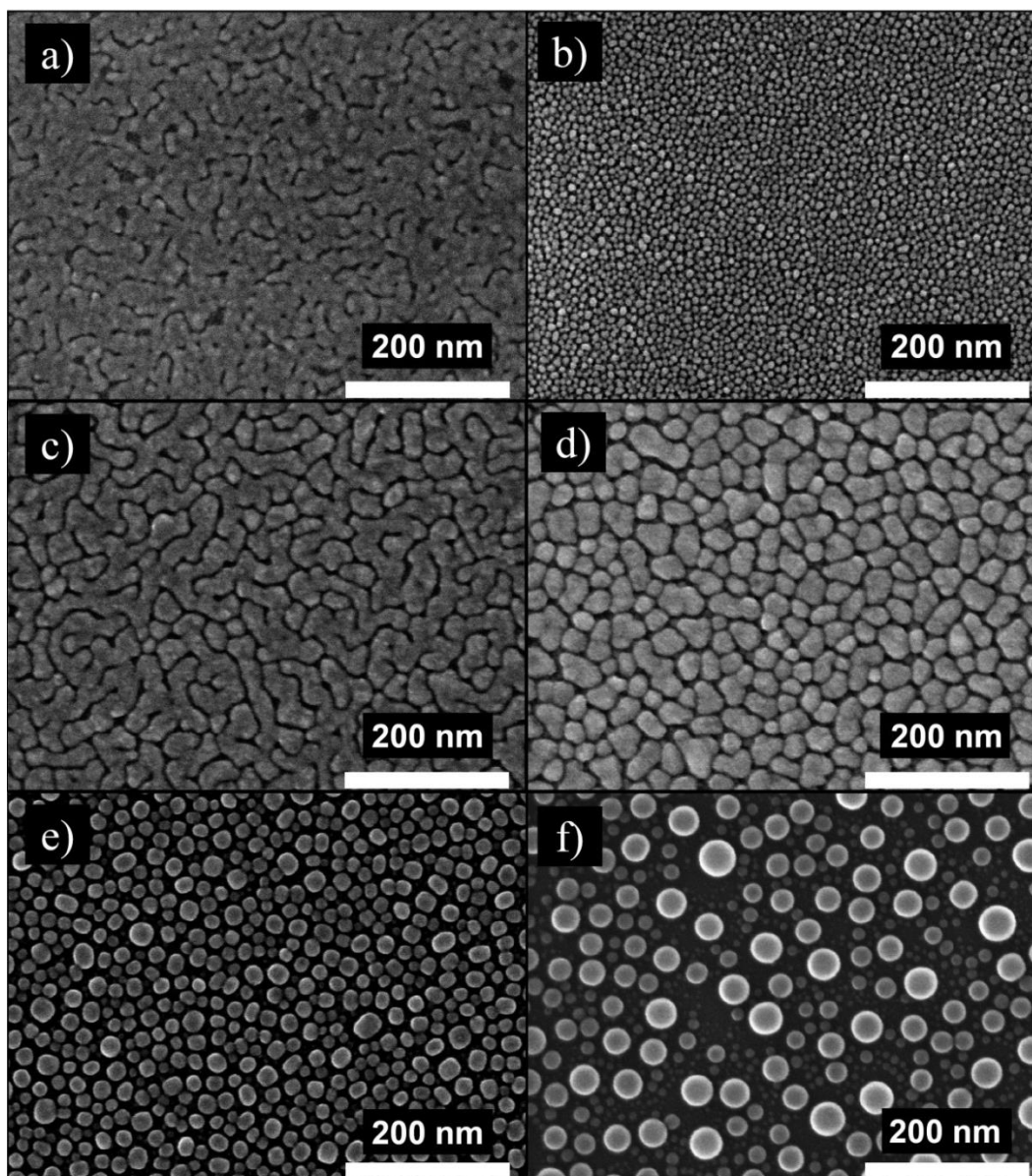


Figure 6.2: Seed layers (thickness = 3.4 nm) of Al (a, b), Cu (c, d), and Sn (e, f). Films on left side grown at room temperature while films shown on right side grown at 250 °C for Cu and Al, and at 105 °C for Sn.

To characterize the accessible morphological range for Sn seeds we deposited 24 samples with varying deposition thicknesses (0.36 nm – 9.5 nm) and substrate temperatures (room temperature – 275 °C). Plan-view SEM images in Figure 6.2 show changing morphology for temperature and varying nominal thickness. Seed

6.3 -Experimental Results

cross sections appear circular, consistent with a hemispherical shape. Smaller seeds are absent near larger seeds, typical of Ostwald ripening processes; larger clusters grow at the expense of smaller clusters. Seed size distributions were characterized for each sample (500–1500 measurements per sample); data for Sn seeds with a nominal thickness up to 4 nm and nominal deposition temperature of 300 °C are shown in Figure 6.3.

6.3 -Experimental Results

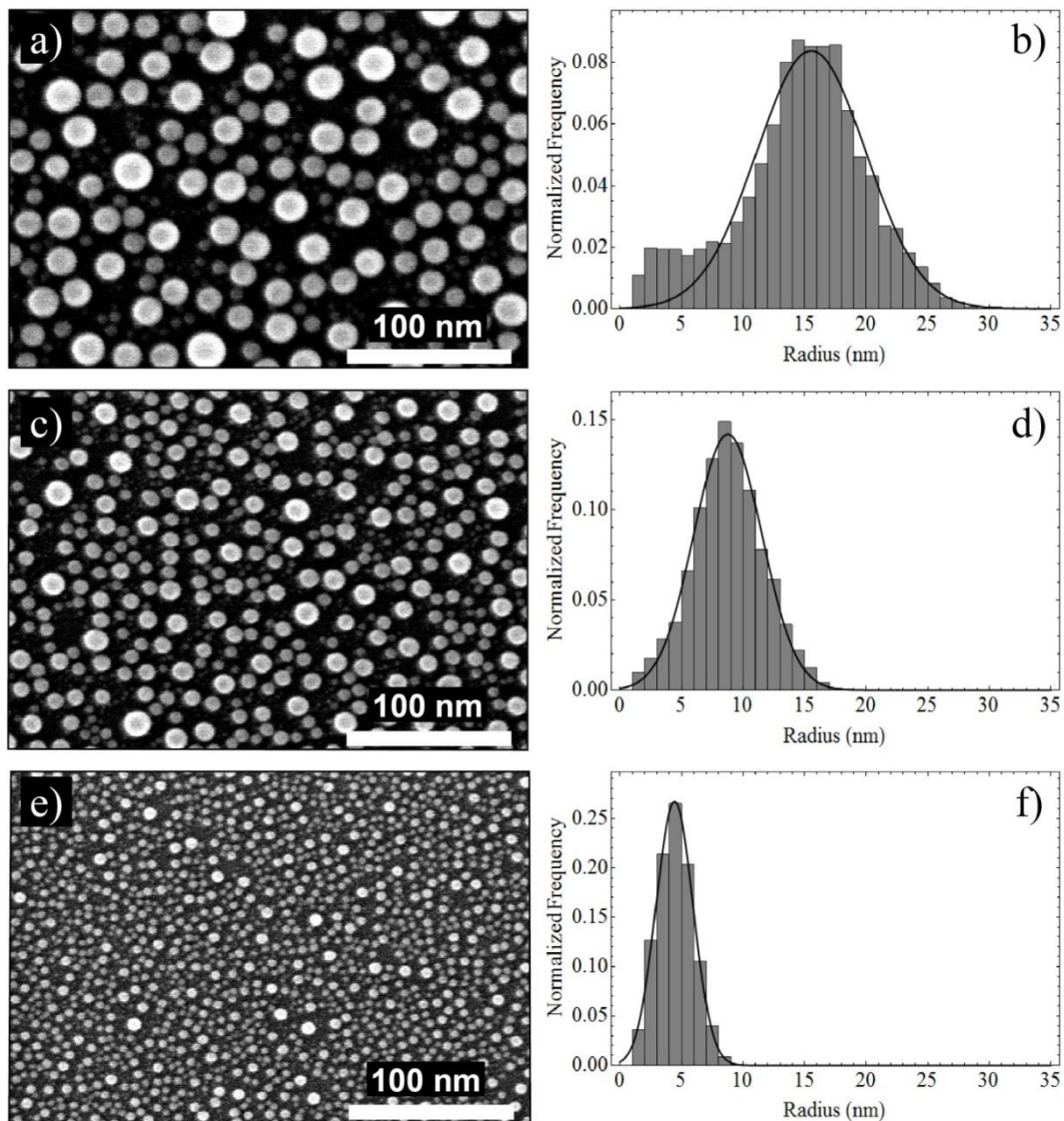


Figure 6.3: Sn seeds layers deposited at a nominal temperature of 300 °C and at different thicknesses (4.7 nm, 3.4 nm, and 0.36 nm for a, b, and c respectively) and their respective size distributions.

Initial inspection of the size histograms revealed a power law distribution of small particles attributed to noise from digital SEM image pixilation, vibration generated aberrations in the SEM image, and noise generated by the Mathematica image processing package. To correctly characterize only the measured particles with physical significance, particles with areas below 3 nm^2 were not included in the size

6.3 -Experimental Results

histograms. A direct distribution fit was used to further reduce the impact of virtual particle noise on the extracted mean and standard deviation from the generated size distributions.

Size distributions for nanoclusters in 3D liquid/vapour matrices undergoing Ostwald ripening have been proposed by Lifshitz-Slyozov [69] and Wagner [67]. Further work by Vengrenovitch et al. [62] refined the distributions for 3D nanoclusters ripening on 2D surfaces. These distributions evolve under very high temperatures for long anneal times (> 8 hr) from symmetrical distributions, towards increasingly asymmetrical distributions. Because our seed layers experience annealing times < 1 hr, we fit our data to a symmetrical Gaussian distribution for simplification.

Nominal film thickness and knowledge of GLAD film uniformity [82], allows us to calculate the seed layer thickness at each wedge. Because seed deposition occurs in parallel, we simultaneously modify effective seed thickness and temperature. To properly represent this dataset, we have aggregated 64 samples from 14 depositions into a seed diameter contour plot using a first order polynomial fit across two dimensions. Average seed separation distance of Sn films as a function of both substrate temperature and thickness are shown in Figure 6.4.

6.3 -Experimental Results

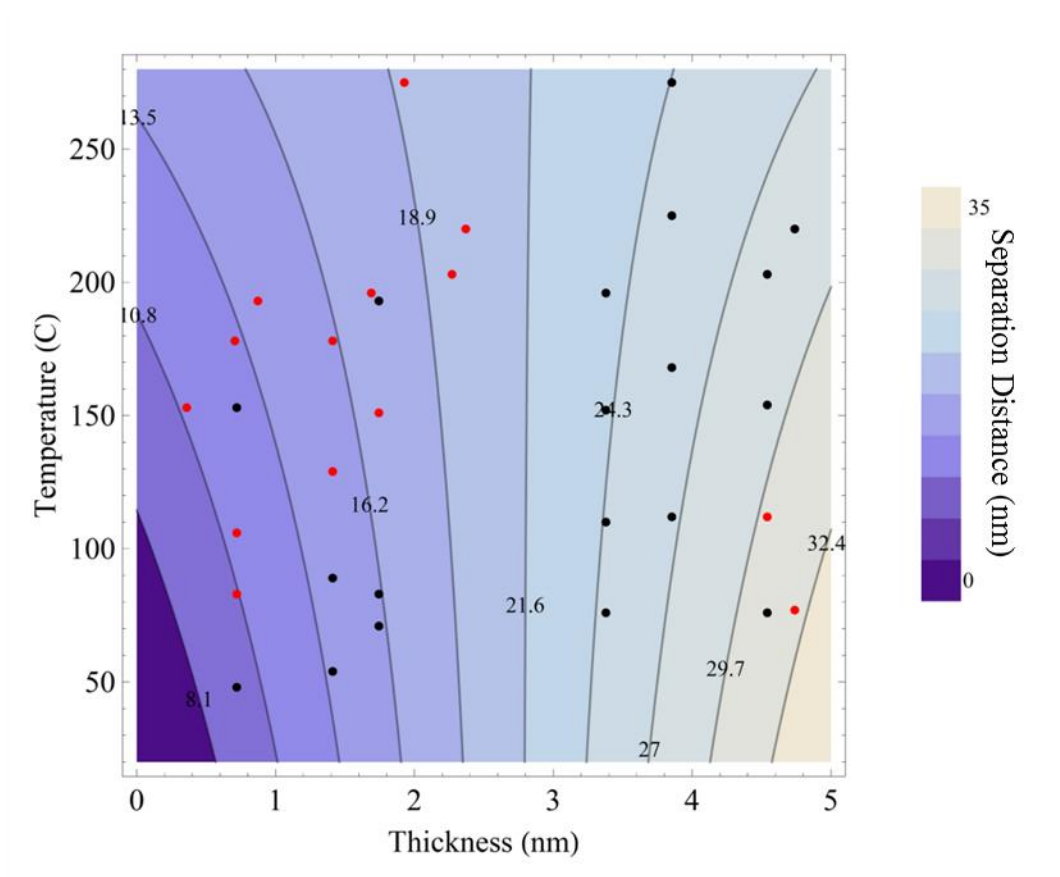


Figure 6.4: Contour plot showing the average Sn seed separation distance at various substrate temperatures and effective thicknesses. Red dots represent data points below the fit, while black dots represent data points above the fit.

From Figure 6.4 we can identify that we deposit more material, the average separation distance between the seeds increases. Higher temperatures produce smaller separation distances in seed layers with nominal thicknesses below 2.8 nm, but larger separation distance in thicker films.

To determine the effect of a seed layer on the microstructure of GLAD thin films, we deposited silicon dioxide vertical posts on both planar Si, as well as planar Si populated with Sn seeds. SEM images of 50 nm SiO₂ vertical posts deposited on

6.3 -Experimental Results

both planar Si and on Si substrates with Sn seeds of various sizes are shown in Figure 6.5.

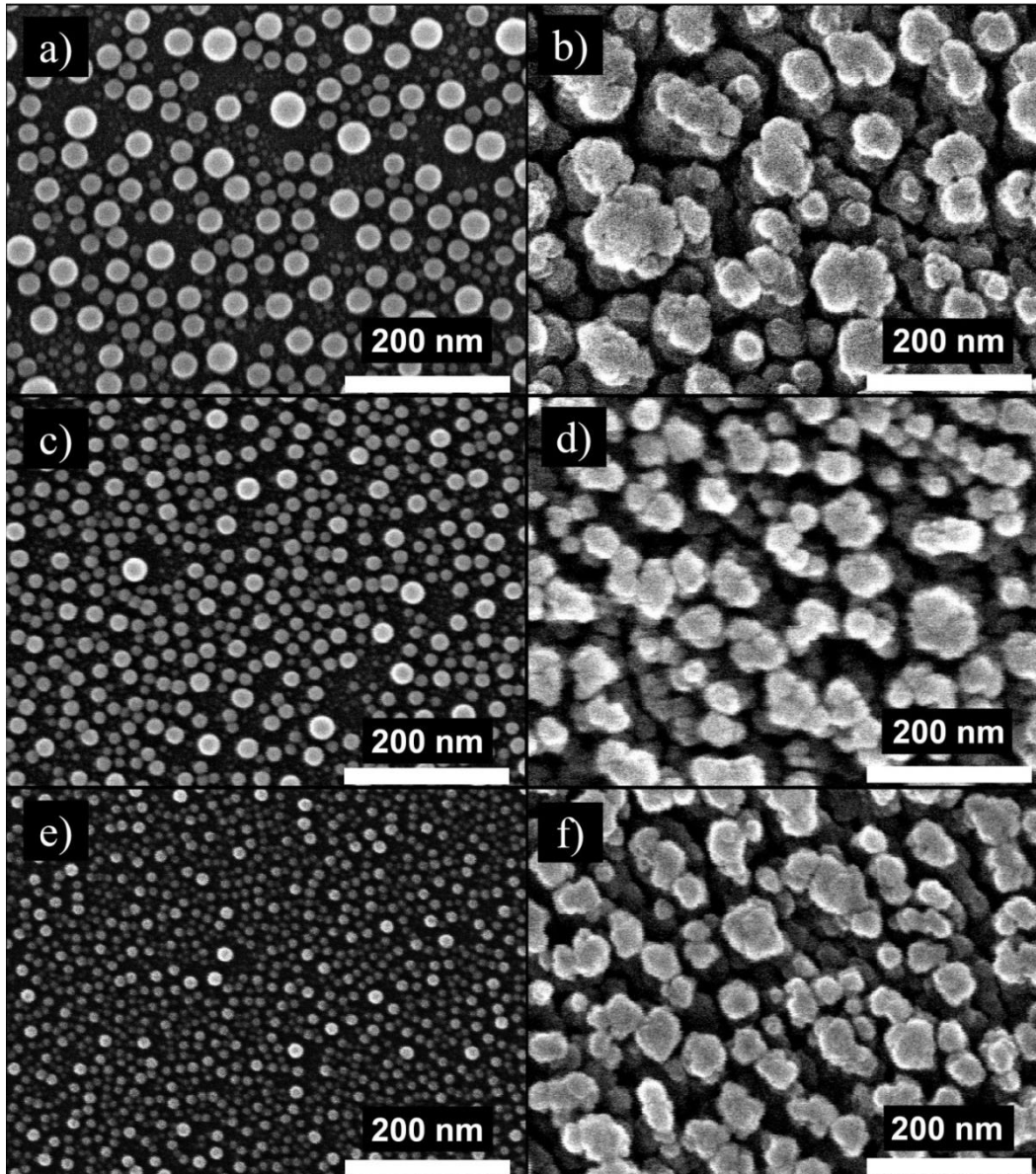


Figure 6.5: SEM micrographs of Sn seeds (left) deposited at $\alpha = 30^\circ$, 60° , and 80° (temperature = 300°C , rate = 0.1 nm s^{-1} , thickness = 4 nm nominal at $\alpha = 30^\circ$) and corresponding SiO_2 vertical posts deposited at $\alpha = 85^\circ$ (room temperature, rate = 1 nm s^{-1} , thickness = 50 nm).

6.3 -Experimental Results

We used autocorrelation to measure average seed and post separations from SEM images of silicon dioxide vertical post films, as well as the underlying Sn seed layers. The autocorrelation script determines the distance of the centroid of each seed or post to the centroid of every other seed or post, and plots the distribution of centroid-centroid distances found in each SEM image. The location of the first maximum in the correlation plot represents the average separation distance between seeds or posts in each image. Figure 6.6 shows a SEM image of a Sn seed layer and the corresponding distributions of separation distances extracted from the image by the autocorrelation script. Figure 6.7 shows average separation for silicon dioxide vertical posts plotted against the average separation for the underlying seeds. The horizontal dotted lines represent the measured unseeded post separation distance for each respective film thickness, with the 500 nm and 1000 nm cases being presented as a band due to the higher amount of error in the measurements at these thicknesses. The linear relationship between the separation distances of the two films suggests that the silicon dioxide vertical posts inherit the locations set by the Sn seeds. The smaller the separation distance of the underlying seed layer, the closer to the control separation distance the seeded post separation distance becomes.

6.3 -Experimental Results

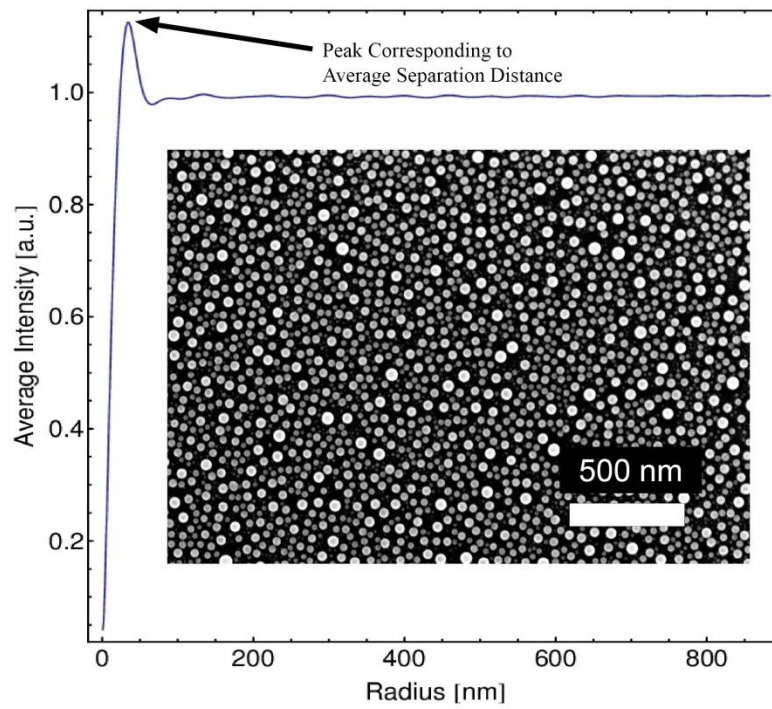


Figure 6.6: A Sn seed layer (thickness = 4.72 nm, $T = 213\text{ }^{\circ}\text{C}$) and the corresponding distribution of separation distances produced by autocorrelation.

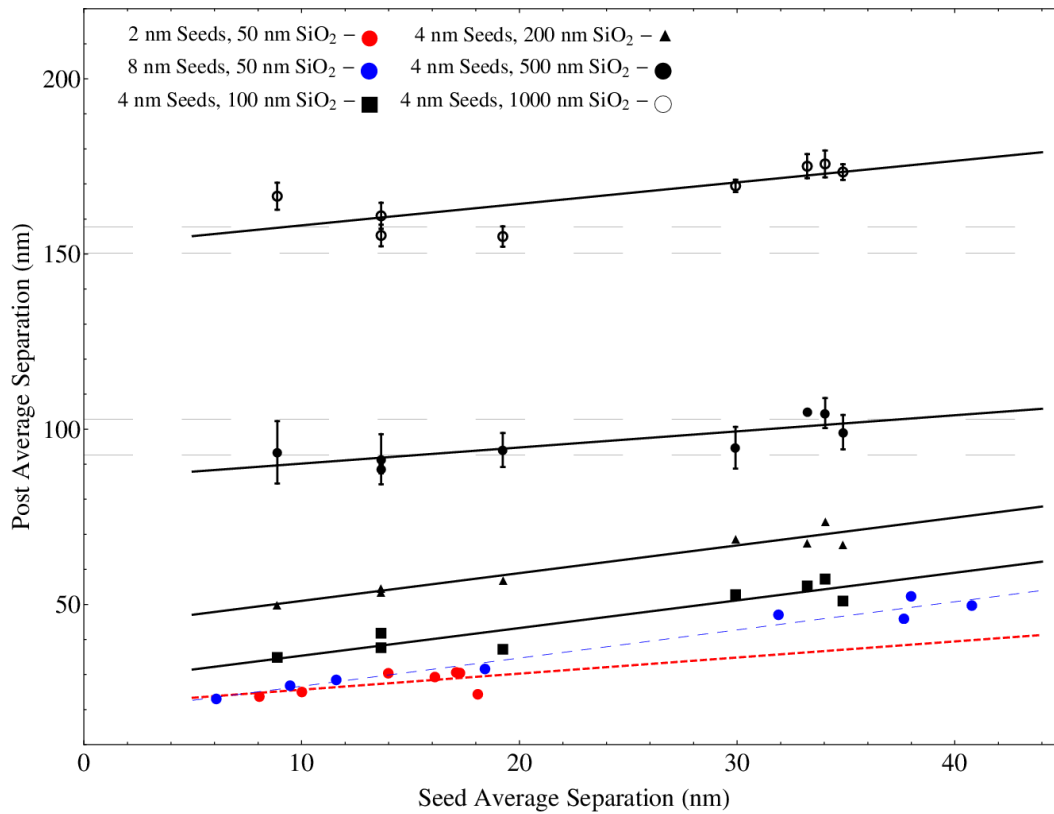


Figure 6.7: Average separation distance for SiO_2 vertical posts and the Sn seeds that they were grown on. Seed layers with a variety of average separation distances were produced using the wedge chuck by depositing Sn to a nominal thickness of 2 nm, 4 nm, and 8 nm. SiO_2 vertical posts were grown to various thicknesses on top of the Sn seed layers. The two regions between dashed lines represent the range of post separation distances found in unseeded SiO_2 vertical post films grown to both 500 nm and 1000 nm. Error bars represent one standard deviation of the mean, which was negligible for vertical posts < 500 nm in thickness.

6.4 - Discussion

Sn seeds appear to form hemispherical caps, as previously observed by Hu *et al.* in Sn/Si systems [70]. This shape is a result of the lower surface energy of metals in contact with the higher surface energy of the native oxide present on the Si substrate surface [96]. The difference between interfacial energies of the two surfaces, in accordance with Young's equation, causes the metal droplets to ball up on the surface forming a large contact angle between droplet and substrate [97-101]. Interfacial energy has been shown to be lower in metals with lower melting

temperatures [102]. Sn has the lowest melting temperature of the materials selected for seeding, explaining why it had the greatest propensity to form the desired seed structure. Our technique for forming hemispherical seeds can be closely compared to the thermal dewetting process commonly used to seed vapour-liquid-solid (VLS) growth of nanowires [103].

Characterization of Sn seed separation distance as a function of film thickness and substrate temperature revealed an interesting divergence of results about a nominal thickness of 2.8 nm. The increase in average separation distance with temperature at lower thicknesses is a net result of increased adatom mobility and increased re-evaporation rates. Adatoms on the substrate surface are able to diffuse further at higher temperatures and therefore are more likely to come together to form a stable nuclei, or join an already existing cluster. This means that large nuclei are more likely to grow, while small nuclei are subject to high dissolution rates governed by the Gibbs-Thomson equation.

As we deposit thicker films, the larger nuclei continue to grow at the expense of smaller nuclei, an effect that is visible in the Sn SEM images where there is a distinct absence of smaller seeds surrounding their larger counterparts. As the substrate temperature increases, the higher rates of adatom diffusion encourages a greater number of stable nuclei to form and grow, populating the surface with a greater number of seeds, and leading to a smaller average seed separation distance than seeds grown at lower temperatures.

SiO₂ vertical posts grown on seeds display a change in structure noticeable to the naked eye as we increase the thickness, and therefore average separation of the

underlying seed layer. As the average separation distance of the seeds increases, the SiO₂ vertical posts become less clumped together, and more isolated, implying an inheritance of Sn seed position. These isolated posts also appear to be larger in diameter than posts grown on smaller seeds. This suggests that the seeds are capturing a larger portion of the SiO₂ flux, and facilitating ballistic shadowing. Many of these posts with larger cross sectional area also appear to have a more circular cross section, meaning that they are receiving flux in a near isometric radial distribution. This is most likely due to the additional height of the hemispherical Sn seed surface being able to capture flux from all φ angles, and avoiding competitive shadowing effects from nearby posts. This would also imply that these seeded posts increase the competitive shadowing of their own neighbours and are more likely to contribute to post extinction.

The inheritance of seed position by SiO₂ posts is confirmed by the linear correlation between seed average separation and post average separation in Figure 6.7, with the higher slopes representing a stronger correlation between the two structured films. Shorter SiO₂ vertical post films correlate stronger than thicker posts, perhaps due to the seeded posts being lost to noise from typical competitive GLAD growth. While linear fits provide an intercept for post average separation, this intercept falls below the measured unseeded post separation distance. This suggests a termination point in the trend of decreasing post separation distance with decreasing seed separation distance, where seeds are either too small to induce ballistic shadowing, or too densely packed to provide adequate protection from competitive growth mechanisms.

6.5 - Chapter Summary

Elevated substrate temperature was used to produce seed layers comprised of hemispherical Sn caps. The low interfacial energy of Sn relative to that of the substrate surface caused the seeds to dewet and form their hemispherical shape. The Ostwald ripening process is attributed with producing larger seeds at the expense of nearby smaller seeds. Sn seed layers were grown to a variety of thicknesses (0.36 nm – 9.5 nm) and at a range of substrate temperatures (room temperature – 275 °C). Size distributions and average separation distances were determined for each sample. SiO₂ vertical posts were grown on top of Sn seed layers to a number of different thicknesses, from which we also extracted average separation distances. The average separation distances for Sn seed layers were then compared with the corresponding SiO₂ vertical posts, which were found to linearly increase together. This correspondence became increasingly erroneous at greater SiO₂ vertical post thicknesses, due to column merging and extinction processes.

Chapter 7

Conclusions:

7.1 - Introduction

The aim of this thesis was to provide greater understanding of the effects of temperature on the glancing angle deposition process, including the development of methods to extend GLAD's capabilities. This thesis has presented a next-generation substrate temperature control system for GLAD. It is capable of heating up to 300 °C and cooling down to -50 °C, while maintaining substrate tilt (α) and rotation (φ) capabilities.

The temperature control system was used for a study on effects of elevated temperature on column tilt angle. Deposition onto heated substrates was also used to demonstrate an *in situ* method for preparing tuneable Sn nucleation layers to act as seeds for the ballistic growth of columnar films.

This chapter will address some of the successes and failures of these actions, as well as identify areas for future work.

7.2 - Design

Chapter 3 highlighted the specific challenges faced when attempting to heat and cool GLAD substrates, including the restrictions of UHV heat transfer. I inferred that temperature measurement from the back surface of the substrate holder was inadequate for determining growth front temperature. To correct this, temperature measurement with a T-type thermocouple was moved to the front surface of a mounted substrate. Furthermore, the installation of a T-type thermocouple

7.2 -Design

feedthrough removed the necessity for cold junction compensation. Heating was achieved using a pair of 250 W bulbs irradiating the front surface of the substrates, rather than from behind the substrate holder. Control of the heating was transferred from a simple Variac transformer to a PID controller receiving temperature feedback from the thermocouple. This heating setup was capable of reaching temperatures of 300 °C and maintaining those temperatures within ± 1 °C. Temperatures exceeding 300 °C could conceivably be achieved using higher power lamps, or by positioning the lamps closer to the substrate holders. Additionally, reducing the thermal mass of the substrate holder would allow for faster heating rates and even higher temperatures still.

This revised heating system could be used to study many temperature dependent structural properties of GLAD films, beyond column inclination angle. These properties include film density, p-value scaling, surface area, and crystallinity.

Improvements to GLAD cooling focused on maintaining the cooling capabilities of the old design, while reducing friction during φ rotation. Also, we once again required that the point of measurement be the front surface of the substrate. We changed the path of heat conduction through graphalloy bushings in direct contact with an oxygen free copper headpiece. The bushings were lubricated using MoS₂ solid lubricant, which allowed for low friction rotation at cryogenic temperatures. Using this new cooling system, we were able to reach temperatures of -50 °C after 64 min. Accurate temperature measurement was facilitated through the use of a dummy headpiece, mimicking the thermal characteristic to the original headpiece while remaining stationary.

7.3 -Effect of Temperature on β

The ability to cool substrates *in situ* with GLAD depositions will enable future ENL/GLAD researchers to deposit low melting point materials that are unable to deposit in a purely ballistic fashion under normal deposition conditions. Many of these low melting temperature materials are metals with high electrical conductivity, such as Cu or Ag. Enabling columnar GLAD grown films using these materials may find application, *e.g.* as electrodes. Researchers may also improve the structure of current materials by using the cooling to further reduce adatom mobilities. Cooling may be used to probe whether or not increasing substrate temperature during deposition is responsible for post broadening, and if so, suppress it.

7.3 - Effect of Temperature on β

The work in Chapter 5 involved exploring the effects of increasing substrate temperature on the column inclination angle, β . Slanted post films grown with five materials—Ti, Cu, Al, Si, and TiO₂—were deposited at both room temperature and elevated temperatures. Unfortunately, Cu, Al and TiO₂ films lost all discernable columnar structure when deposited at selected substrate temperatures. Additional depositions performed at lower substrate temperatures may have revealed a change in column inclination angle while remaining in a regime where columnar growth was still possible. Si slanted posts grown at $\alpha = 80^\circ$ grew at column inclination angles of $50.97^\circ \pm 1.32^\circ$ and $50.24^\circ \pm 1.77^\circ$ when deposited on substrate at room temperature and 300 °C respectively. Ti slanted posts deposited at 300 °C when compared to room temperature showed an average increase in β of $6.4^\circ \pm 2.2^\circ$, measured from films deposited at $\alpha = 30^\circ, 40^\circ, 50^\circ, 60^\circ, 70^\circ, \text{ and } 80^\circ$.

The findings that show increasing column inclination temperature with increasing substrate temperature challenge previous work by Lichter *et al.* [22] and Nakhodkin *et*

al. [23] who found the opposite to be true, both experimentally and theoretically. Like many other GLAD growth parameters, column inclination angle has been shown to be a material-dependent property. It would therefore be unsurprising if different material systems shared little congruency in their response to changes in substrate temperature. It would prove prudent to seek further examination of the effect of substrate temperature on β , with greater resolution in temperature space, and on a wider breadth of materials. While heating induced an upward shift in β , cooling could provide the opposite effect, revealing a greater sense of mechanism. Perhaps the relationship between substrate temperature and column inclination angle is monotonic only at our observed temperature range.

7.4 - GLAD Nucleation

In Chapter 6, I developed a method for producing Sn seed layers with tuneable diameter and separation distance distributions through manipulation of deposition rate/thickness and substrate temperature. I used autocorrelation to characterize the impact on separation distance of SiO₂ vertical posts deposited to various thicknesses on top of Sn seed layers. A linear correlation between Sn seed separation and SiO₂ post separation was found, indicating an inheritance of seed position by the corresponding vertical post film. Stronger correlation between the two films, indicated by a greater slope, was found at shorter post heights. I suspect that in thicker SiO₂ films, competitive growth processes eliminate some of the signal of preference seen in shorter films. Perhaps more refined deposition algorithms combined with vertical post deposition parameters designed to reduce competitive processes may enable the same degree of inheritance in thicker films as was seen in thinner ones.

7.4 -GLAD Nucleation

Though our method of seeding does not provide absolute control over the position of columns, we have shown the ability to sufficiently perturb the stochastic processes involved in column nucleation. This kind of change in structure may find application in fields where performance is based on film properties such as porosity, column size, or column spacing. Analyte motion thin film chromatography has been shown to be a function of column spacing, which could be tuned using our seeding method [41]. Optically birefringent films have been grown through GLAD for use as light polarization filters [104]. Birefringence is a result of anisotropic refractive indices parallel and perpendicular to column orientation. The degree of anisotropy is a function of inter-column spacing, which could be further tuned using our seeding technique.

Bibliography:

- [1] K. Robbie, J. Sit, M. J. Brett, "Advanced techniques for glancing angle deposition", *Journal of Vacuum Science and Technology B*, Vol. 16, Issue 3, pp. 1115-1122, 1998.
- [2] D. Gish, et al., "Morphology of periodic nanostructures for photonic crystals grown by glancing angle deposition", *Photonics and Nanostructures – Fundamentals and Applications*, Vol. 4, pp. 23-29, 2006.
- [3] H. Poppa, "Progress in the Continuous Observation of Thin-Film Nucleation and Growth Process by Electron Microscopy", *Journal of Vacuum Science and Technology*, Vol. 2, Issue 4, 1965.
- [4] B. Lewis, D. S. Campbell, "Nucleation and Initial-Growth Behavior of Thin-Film Deposits", *Journal of Vacuum Science and Technology*, Vol. 4, Issue 5, pp. 209-218, 1967.
- [5] C. Ratsch, J. A. Venables, "Nucleation and the early stages of thin film growth", *Journal of Vacuum Science and Technology A*, Volume 21, Issue 5, pp. S96-S109, 2003.
- [6] R. Messier, et al., "Origin and evolution of sculptured thin films", *Journal of Vacuum Science and Technology A*, Volume 18, Issue 4, pp 1538-1545, 2000.
- [7] K. Robbie, M. J. Brett, "Sculptured thin films and glancing angle deposition: Growth mechanisms and applications", *Journal of Vacuum Science and Technology A*, Vol. 15, Issue 3, pp. 1460-1465, 1997.
- [8] M. M. Hawkeye, et al., "Glancing angle deposition: Fabrication, properties, and applications of micro- and nanostructured thin films", *Journal of Vacuum Science and Technology A*, Vol. 25, Issue 5, pp. 1317-1335, 2007.
- [9] J. Sit, et al., "Thin film microstructure control using glancing angle deposition by sputtering", *Journal of Materials Research*, Vol. 14, No. 4, 1999.
- [10] G. Micocci, A. Tepore, "Electrical properties of vacuum-deposited polycrystalline InSe thin films", *Solar Energy Materials*, Vol. 22, Issue 2-3, pp. 215-222, 1991.
- [11] B. A. Movchan, A. V. Demchishin, "Study of Structure and Properties of Thick Vacuum Condensates of Nickel, Titanium, Tungsten, Aluminum Oxide and Zirconium Dioxide", *Physics of Metals and Metallography-USSR*, Vol. 28, Issue 4, pp. 83, 1969.

Bibliography:

- [12] J.V. Sanders, in: J.R. Anderson Ed., *Chemisorption and Reactions on Metallic Films*, Academic Press, London, 1971.
- [13] H. E. Julyan, et al., "Ice films follow structure zone model morphologies", *Thin Solid Films*, Vol. 518, Issue 12, 2010.
- [14] C. M. Zhou, et al., "Growth competition during glancing angle deposition of nanorod honeycomb arrays", *Applied Physics Letters*, Vol. 90, Issue 9, pp. 90-92, 2007.
- [15] C. M. Zhou, et al., "Development of two-level porosity during glancing angle deposition", *Journal of Applied Physics*, Volume 103, Issue 1, 2008.
- [16] C Khare, et al., "Growth temperature altered morphology of Ge nanocolumns", *Physica Status Solidi A*, Volume 208, Issue 4, pp. 851-856, 2011.
- [17] A. T. Wu, et al., "Capacitive SiO₂ humidity sensors with novel microstructures", *Sensors and Materials*, Volume 11, Issue 8, pp. 493-505, 1999.
- [18] J M Nieuwenhuizen, H B Haanstra, *Philips Tech Rev.* 27, (1966)87.
- [19] H. Fujiwara, et al., "Comment on the Tangent Rule", *Thin Solid Films*, Vol. 163, pp. 387-391, 1988.
- [20] R N Tait, et al., "Modeling and Characterization of Columnar Growth in Evaporated-Films", *Thin Solid Films*, Vol. 226, Issue 2, pp. 196-201, 1993.
- [21] A. Hagemeyer, et al., "Crystallographic Texture and of Obliquely Deposited Co-Cr Magnetic Thin-Films on Flexible Polymeric Substrates", *Thin Solid Films*, Vol. 230, Issue 2, pp. 199-202, 1993.
- [22] S. Lichter, J. Chen, "Model for Columnar Microstructure of Thin Solid Films", *Physical Review Letters*, Vol. 56, Issue 13, pp. 1396-1399, 1986.
- [23] N. G. Nakhodkin, A. I. Shalderv, "Effect of Condensation Conditions on Growth of Columnar Crystallites in Aluminum Films", *Soviet Physics Solid State*, Vol. 13, Issue 7, pp. 1627-&, 1972.
- [24] T. Hashimoto, et al., "Columnar Structure and Texture of Iron Films Evaporated at Oblique-Incidence", *Thin Solid Films*, Vol. 91, Issue 2, pp. 145-154, 1982.
- [25] I. Hodgkinson, et al., "Empirical equations for the principle refractive indices and column angle of obliquely deposited films of tantalum oxide, titanium oxide, and zirconium oxide", *Applied Optics*, Vol. 37, Issue 13, pp. 2653-2659, 1998.

- [26] J. M. Garcia-Martin, et al., "Tilt angle control of nanocolumn grown by glancing angle sputtering at variable argon pressures", *Applied Physics Letters*, Vol. 97, Issue 17, 2010.
- [27] D. A. Gish, et al., "Enhanced control of morphology in thin film nanostructure arrays", 2006 IEEE Conference on Emerging Technologies – Nanoelectronics, pp. 447-451, 2006.
- [28] J. B. Sorge, M. J. Brett, "Film morphology modification in ion-assisted glancing angle deposition", *Thin Solid Films*, Vol. 519, Issue 4, pp. 1356-1360, 2010.
- [29] K. Robbie, et al., "Inhomogeneous thin film optical filters fabricated using glancing angle deposition", *Electronics Letters*, Vol. 33, Issue 13, pp. 1213-1214, 1997.
- [30] K. Kaminska, et al., "Rugate filters grown by Glancing Angle Deposition", *Proc. Of the SPIE*, Vol. 5833, pp. 633-639, 2002.
- [31] K. Kaminska, et al., "Vacuum evaporated porous silicon photonic interference filters", *Applied Optics*, Vol. 42, Issue 20, pp. 4212-4219, 2003.
- [32] A. C. van Popta, et al., "Gradient-index narrow-bandpass filter fabricated with glancing-angle deposition", *Optics Letters*, Vol. 29, Issue 21, pp. 2545-2547, 2004.
- [33] Y. J. Park, et al., "Wideband circular polarization reflector fabricated by glancing angle deposition", *Optics Express*, Vol. 16, Issue 8, pp. 5186-5192, 2008.
- [34] J. Sit, *Thin film / liquid crystal composite optical materials and devices*, PhD Thesis, University of Alberta, 2002.
- [35] B. Dick, et al., "Periodic magnetic microstructures by glancing angle deposition", *Journal of Vacuum Science & Technology A*, Vol. 18, Issue 4, pp. 1838-1844, 2000.
- [36] F. Liu, et al., "The magnetic properties of cobalt films produced by glancing angle deposition", *IEEE Transactions on magnetics*, Vol. 36, Issue 5, pp. 2939-2941, 2000.
- [37] J.J. Steele, et al., "Sub-second humidity sensing based on nanostructured narrow-bandpass optical filters", *Materials Research Society Symposium Proceedings*, Vol. 915, pp. 231-236, 2006.
- [38] K. D. Harris, et al., "High-speed porous thin film humidity sensors," *Electrochem. Solid-State Lett*, Vol. 5, no. 11, pp. H27–H29, 2002.

Bibliography:

- [39] J.J. Steele, et al., “Capacitive humidity sensors with high sensitivity and subsecond response times”, IEEE Sensors Journal, Vol. 7, Issue 5-6, pp. 955-956, 2007.
- [40] J.J. Steele, et al., “Nanostructured metal oxide thin films for humidity sensors,” IEEE Sensors J., vol. 8, no. 8, pp. 1422–1429, 2008.
- [41] L. Bezuidenhout, M. J. Brett, “Ultrathin layer chromatography on nanostructured thin films”, Vol. 1183, Issue 1-2, pp.179-185, 2008.
- [42] S. R. Jim, et al., “Engineered Anisotropic Microstructures for Ultrathin-Layer Chromatography”, Analytical Chemistry, Vol. 82, Issue 12, pp. 5349-5356, 2010.
- [43] J. G. Van Dijken, et al., “Controlled nanostructuring of CuPc thin films via glancing angle deposition for idealized organic photovoltaic architectures”, Journal of Materials Chemistry, Vol. 21, Issue 4, pp. 1013-1019, 2011.
- [44] N.J. Podraza, et al., “Transparent conducting oxide sculptured thin films for photovoltaic applications”, MRSS Proceedings, Vol. 865, pp273-278, 2005.
- [45] N.J. Gerein, et al., “Nanostructured Titanium Dioxide/Polythiophene Photovoltaic Devices”, IEEE Photovoltaic Specialist Conference, Vol. 1-4, pp. 1116-1121, 2008.
- [46] Y. Zheng, et al., “Organic photovoltaic cells with vertically aligned crystalline molecular nanorods”, Organic Electronics, Vol. 10, Issue 8, pp. 1621-1625, 2009.
- [47] D. A. Rider, et al., “Indium tin oxide nanopillar electrodes in polymer/fullerene solar cells”, Nanotechnology, Vol. 22, Issue 8, 2011.
- [48] J. A. Venables, et al., “Nucleation and Growth of Thin-Films”, Reports on Progression in Physics, Vol. 47, Issue 4, pp. 399-459, 1984.
- [49] M. Ohring, *Materials Science of Thin Films 2nd Edition*, Academic Press, 2002. pp. 373-388.
- [50] G. K. Hubler, J. A. Sprague, “Energetic particles in PVD technology: Particle-surface interaction processes and energy-particle relationships in thin film deposition”, Surface & Coatings Technology, Vol. 81, Issue 1, pp. 29-35, 1996.
- [51] R. Gomer, “Diffusion of Adsorbates on Metal-Surfaces”, Reports on Progress in Physics, Vol 53, Issue 7, pp. 917-1002, 1990.
- [52] A.D. Leclaire, “Diffusion of Metals in Metals”, Progress in Metal Physics, Vol. 1, pp. 306-379, 1949.

Bibliography:

- [53] A.D. Leclaire, "The Theory of D_0 in the Arrhenius Equation for Self-Diffusion in Cubic Metals", *ACTA Metallurgica*, Vol. 1, Issue 4, pp. 438-447, 1953.
- [54] A.M. Brown, M.F. Ashby, "Correlations for Diffusion Constants", *ACTA Metallurgica*, Vol. 28, Issue 8, pp. 1085-1101, 1980.
- [55] K. Reichelt, "Nucleation and Growth of Thin-Films", *Vacuum*, Vol. 38, Issue 12, pp. 1083-1099, 1988.
- [56] L. Abelmann, C. Lodder, "Oblique evaporation and surface diffusion", *Thin Solid Films*, Vol. 305, Issue 1-2, pp. 1-21, 1997.
- [57] C. Ratsch, J.A. Venables, "Nucleation theory and the early stages of thin film growth", *Journal of Vacuum Science and Technology A*, Vol 21, Issue 5, 2003.
- [58] D. Turnbull, "Formation of Crystal Nuclei in Liquid Metals", *Journal of Applied Physics*, Vol. 21, Issue 10, pp. 1022-1028, 1950.
- [59] F.M. Fowkes, "Attractive Forces at Interfaces", *Industrial and Engineering Chemistry*, Vol. 56, Issue 12, pp. 40-&, 1964.
- [60] J. Lothe, "Reconsiderations of Nucleation Theory", *Journal of Chemical Physics*, Vol. 36, Issue 8, pp. 2080-&, 1962.
- [61] D. A. Porter, K. E. Easterling, *Phase Transformations in Metals and Alloys – Second Edition*, Taylor & Francis Group, 2004, pp. 185-187.
- [62] R.D. Vengrenovitch, "On the Ostwald Ripening Theory", *Acta Metall.*, Vol. 30, pp. 1079-1086, 1982.
- [63] M. Zinke-Allmang, et al., "Clustering on surfaces", *Surface Science Reports*, Vol. 16, Issue 8, pp. 377-463, 1992.
- [64] M. Zinke-Allmang, "Phase separation on solid surfaces: nucleation, coarsening and coalescence kinetics", *Thin Solid Films*, Vol. 346, pp. 1-68, 1999.
- [65] J. Garside, et al., "On size-dependent crystal growth", *Industrial and Engineering Chemistry Fundamentals*, Vol. 15, Issue 3, pp. 230-233, 1976.
- [66] C.A. Johnson, "Generalization of the Gibbs-Thomson equation", *Surface Science*, Vol. 3, Issue 5, pp. 429-444, 1965.
- [67] B.K. Chakraverty, "Grain Size Distribution in Thin Films—1. Conservative Systems", *J. Phys. Chem. Solids*, Vol. 28, pp. 2401-2412, 1967.

Bibliography:

- [68] J. Wang, D.R. Flanagan, "General Solution for Diffusion-Controlled Dissolution of Spherical Particles. 1. Theory", *Journal of Pharmaceutical Sciences*, Vol. 88, No. 7, 1999.
- [69] I.M. Lifshitz, V.V. Slyozov, "The kinetics of precipitation from supersaturated solid solutions", *Journal of Physics and Chemistry of Solids*, Vol. 19, Issues 1-2, pp. 35-50, 1961.
- [70] Q. Hu, M. Zinke-Allmang, "Atomic force microscopy study of the early stages of Sn phase separation on Si(111) surfaces", *Journal of Vacuum Science and Technology A*, Vol. 20, Issue 3, 2002.
- [71] K. Shorlin, et al., "Fundamental problems concerning three dimensional clustering on surfaces", *Physica A*, Vol. 261, pp. 248-265, 1998.
- [72] G.R. Carlow, "Ostwald ripening on surfaces when mass conservation is violated: spatial cluster patterns", *Physica A*, Vol. 239, pp. 65-77, 1997.
- [73] P.P. Lau, et al., "Classification of Palladium Nucleation Processes Based on Nucleus Size Distribution", *Journal of Electrochemical Society*, Vol. 151, Issue 6, 2004.
- [74] R. D. Vengrenovich, et al., "Generalized Lifshits-Slezov-Wagner distribution", *Journal of Experimental and Theoretical Physics*, Vol. 104, Issue 6, pp. 906-912, 2007.
- [75] C.L. Tien, G. Chen, "Challenges in Microscale Conductive and Radiative Heat Transfer", *Journal of Heat Transfer*, Vol. 116, pp. 799-807, 1994
- [76] M. R. Hilton, et al., "Structural and Tribological Studies of MoS₂ Solid Lubricant Films Having Tailored Metal-Multilayer Nanostructures", *Surface & Coatings Technology*, Vol. 53, Issue 1, pp. 13-23, 1992.
- [77] C. Donnet, et al., "Superlow friction of oxygen-free MoS₂ coatings in ultrahigh-vacuum", *Surface & Coatings Technology*, Vol. 62, Issue 1-3, pp. 406-411, 1993.
- [78] Jet Lube, Moly Mist: Technical Data Sheet, Viewed at http://www.jetlubecanada.com/pages/Moly_Mist.html.
- [79] H. E. Sliney, "Solid lubricant materials for high temperatures – a review", *Tribology International*, Vol. 15, Issue 5, pp. 303-315, 1982.
- [80] M.J. Viens. NIST ITS-90 Thermocouple Database. Viewed at <http://srdata.nist.gov/its90/main/>.

Bibliography:

- [81] INFICON, Technical Note: 10000004, “Temperature Coefficient of Maxtek Monitor Crystals”, Available Online at <http://www.inficonthinfilmd deposition.com/en/quartzcrystals.html>.
- [82] N.G. Wakefield, J.C. Sit, “On the uniformity of films fabricated by glancing angle deposition”, *Journal of Applied Physics*, Vol. 109, 2011.
- [83] D.A. Griffith, “Spatial Autocorrelation”, Accessed online at Elsevier, <http://www.elsevierdirect.com/brochures/hugy/SampleContent/Spatial-Autocorrelation.pdf>
- [84] D X Ye, et al., “Manipulating the column tilt angles of nanocolumnar films by glancing-angle deposition”, *Nanotechnology*, Vol. 13, Issue 5, pp. 615-618, 2002.
- [85] C. Khare, et al., “Influence of substrate temperature on glancing angle deposited Ag nanorods”, *Journal of Vacuum Science and Technology A.*, Vol. 28, No. 4, 2010.
- [86] D. Deniz, R. J. Lad, “Temperature threshold for nanorod structuring of metal and oxide films grown by glancing angle deposition”, *Journal of Vacuum Science and Technology A.*, Vol. 29, Issue 1, 2011.
- [87] C. Patzig, B. Rauschenbach, “Temperature effect on the glancing angle deposition of Si sculptured thin films”, *Journal of Vacuum Science and Technology A.*, Vol. 26, No. 4, 2008.
- [88] M. Malac, et al., “Fabrication of submicrometer regular arrays of pillars and helices”, *Journal of Vacuum Science & Technology B*, Vol. 17, Issue 6, pp. 2671-2674, 1999.
- [89] D.A. Gish, et al., “Enhanced control of morphology in thin film nanostructure arrays”, 2006 IEEE Conference on Emerging Technologies – Nanoelectronics, pp. 447-451, 2006.
- [90] M.A. Summers, M.J. Brett, “Optimization of periodic column growth in glancing angle deposition for photonic crystal fabrication”, *Nanotechnology*, Vol. 19, Issue 41, 2008.
- [91] J.D. Krabbe, et al., “Square spiral photonic crystal with visible bandgap”, *Journal of Applied Physics*, Vol. 111, Issue 6, 2012.
- [92] S.V. kesapragada, D. Gall, “Two-component nanopillar arrays grown by Glancing Angle Deposition”, *Thin Solid Films*, Vol. 494, Issue 1-2, pp. 234-239, 2006.

Bibliography:

- [92] C.M. Zhou, D. Gall, "Surface patterning by nanosphere lithography for layer growth with ordered pores", *Thin Solid Films*, Vol. 516, Issue 2-4, pp. 433-437, 2007.
- [94] M.T. Taschuk, et al., "Optical characterization of pseudo-ordered nanostructured thin films", *Physica Status Solidi C*, Vol. 6, pp. S127-S130, 2009.
- [95] C. Liu, J. Lue, "Second harmonic generation from closed packed hexagonal of nano-nickel arrays", *Optics Communications*, Vol. 280, Issue 2, pp. 477-481, 2007.
- [96] V. D. Jonghe, D. Chatain, "Experimental Study of Wetting Hysteresis on Surfaces with Controlled Geometrical and/or Chemical Defects", *Acta Metallurgica et Materialia*, Vol. 43, Issue 4, pp. 1505-1515, 1995.
- [97] A. Krupski, "Growth of Sn on Mo(110) studied by AES and STM", *Surface Science*, Vol. 605, pp. 1291-1297, 2011.
- [98] X. Zhao, et al., "Growth research of Sn nanoparticles deposited on Si(001) substrate by solid phase epitaxy", *Applied Surface Science*, Vol. 256, pp. 6427-6432, 2010.
- [99] M. K. Dawood, et al., "Mimicking Both Petal and Lotus Effects on a Single Silicon Substrate by Tuning the Wettability of Nanostructured Surfaces", *Langmuir*, Vol. 27, Issue 7, pp. 4126-4133, 2011.
- [100] T. Ichinokawa, et al., "Behaviors of small molten metal islands on several substrates", *Journal of Analytical Atomic Spectrometry*, Vol. 14, pp. 405-408, 1999.
- [101] P. Shen, et al., "Reactive Wetting of SiO₂ Substrates by Molten Al", *Metallurgical and Materials Transactions A*, Vol. 35A, pp. 583-588, 2004.
- [102] S. Blairs, U. Joasoo, "On the relationship between melting temperature, nearest-neighbor separation, and surface free energy of liquid and solid metals", *Journal of Colloid and Interface Science*, Vol. 79, Issue 2, pp. 373-380, 1981.
- [103] R. R. Kumar, et al., "Growth of silicon nanowires by electron beam evaporation using indium catalyst", *Materials Letters*, Vol. 66, pp. 110-112, 2012.
- [104] V. Leontyev, et al., "Numerical simulation and rational design of optically anisotropic columnar films", *Photonic and Phononic Properties of Engineered Nanostructures*, *Proceedings of SPIE*, Vol. 7946, 2011.